Astronomy
&
Astrophysics

The feedback of an HC HII region on its parental molecular core

The case of core A1 in the star-forming region G24.78+0.08

L. Moscadelli[1], V. M. Rivilla[1], R. Cesaroni[1], M. T. Beltrán[1], Á. Sánchez-Monge[2], P. Schilke[2], J. C. Mottram[3],
A. Ahmadi[3], V. Allen[4,5], H. Beuther[3], T. Csengeri[6], S. Etoka[7], D. Galli[1], C. Goddi[8,9], K. G. Johnston[10],
P. D. Klaassen[11], R. Kuiper[12], M. S. N. Kumar[13,14], L. T. Maud[8], T. Möller[2], T. Peters[15], F. Van der Tak[4,5], and S. Vig[16]

[1] INAF-Osservatorio Astrofisico di Arcetri, Largo E. Fermi 5, 50125 Firenze, Italy
   e-mail: mosca@arcetri.astro.it
[2] I. Physikalisches Institut, Universität zu Köln, Zülpicher Str. 77, 50937 Köln, Germany
[3] Max Planck Institut for Astronomy, Königstuhl 17, 69117 Heidelberg, Germany
[4] SRON Netherlands Institute for Space Research, Landleven 12, 9747 AD Groningen, The Netherlands
[5] Kapteyn Astronomical Institute, University of Groningen, 9700 AV Groningen, The Netherlands
[6] Max Planck Institut für Radioastronomie, Auf dem Hügel 69, 53121 Bonn, Germany
[7] Jodrell Bank Centre for Astrophysics, The University of Manchester, Alan Turing Building, Manchester M13 9PL, UK
[8] Leiden Observatory, Leiden University, PO Box 9513, 2300 RA Leiden, The Netherlands
[9] Department of Astrophysics/IMAPP, Radboud University, PO Box 9010, 6500 GL Nijmegen, The Netherlands
[10] School of Physics and Astronomy, University of Leeds, West Yorkshire, Leeds LS2 9JT, UK
[11] UK Astronomy Technology Centre, Royal Observatory Edinburgh, Blackford Hill, Edinburgh EH9 3HJ, UK
[12] Institute of Astronomy and Astrophysics, University of Tübingen, Auf der Morgenstelle 10, 72076 Tübingen, Germany
[13] Instituto de Astrofísica e Ciências do Espaço, Universidade do Porto, CAUP, Rua das Estrelas, 4150-762 Porto, Portugal
[14] Centre for Astrophysics, University of Hertfordshire, Hatfield AL10 9AB, UK
[15] Max-Planck-Institut für Astrophysik, Karl-Schwarzschild-Str. 1, 85748 Garching, Germany
[16] Indian Institute of Space Science and Technology, Thiruvananthapuram 695547 Kerala, India

Received 22 January 2018 / Accepted 21 March 2018

ABSTRACT

Context. G24.78+0.08 is a well known high-mass star-forming region, where several molecular cores harboring OB young stellar objects are found inside a clump of size $\approx$1 pc. This article focuses on the most prominent of these cores, A1, where an intense hypercompact (HC) HII region has been discovered by previous observations.
Aims. Our aim is to determine the physical conditions and the kinematics of core A1, and study the interaction of the HII region with the parental molecular core.
Methods. We combine ALMA 1.4 mm high-angular resolution ($\approx$0.′′2) observations of continuum and line emission with multi-epoch Very Long Baseline Interferometry data of water 22 GHz and methanol 6.7 GHz masers. These observations allow us to study the gas kinematics on linear scales from 10 to 10^4 au, and to accurately map the physical conditions of the gas over core A1.
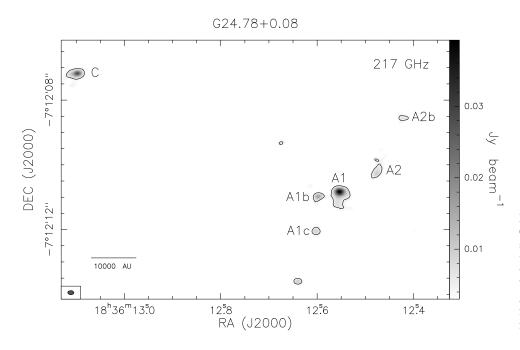*Results.* The 1.4 mm continuum is dominated by free-free emission from the intense HC HII region (size $\approx$1000 au) observed to the North of core A1 (region A1N). Analyzing the H30α line, we reveal a fast bipolar flow in the ionized gas, covering a range of LSR velocities ($V_{\rm LSR}$) of $\approx$60 km s^{-1}. The amplitude of the $V_{\rm LSR}$ gradient, 22 km s^{-1} mpc^{-1}, is one of the highest so far observed towards HC HII regions. Water and methanol masers are distributed around the HC HII region in A1N, and the maser three-dimensional (3D) velocities clearly indicate that the ionized gas is expanding at high speed ($\geq$200 km s^{-1}) into the surrounding molecular gas. The temperature distribution (in the range 100–400 K) over core A1, traced with molecular (CH$_3$OCHO, ^{13}CH$_3$CN, ^{13}CH$_3$OH, and CH$_3$CH$_2$CN) transitions with level energy in the range 30 K $\leq E_u/k \leq$ 300 K, reflects the distribution of shocks produced by the fast-expansion of the ionized gas of the HII region. The high-energy (550 K $\leq E_u/k \leq$ 800 K) transitions of vibrationally excited CH$_3$CN are likely radiatively pumped, and their rotational temperature can significantly differ from the kinetic temperature of the gas. Over core A1, the $V_{\rm LSR}$ maps from both the 1.4 mm molecular lines and the 6.7 GHz methanol masers consistently show a $V_{\rm LSR}$ gradient (amplitude $\approx$0.3 km s^{-1} mpc^{-1}) directed approximately S–N. Rather than gravitationally supported rotation of a massive toroid, we interpret this velocity gradient as a relatively slow expansion of core A1.

Key words. techniques: interferometric – masers – ISM: jets and outflows – ISM: molecules – radio continuum: ISM

1. Introduction

Our knowledge of how massive ($\geq 8\ M_\odot$) stars form is still incomplete, and that is particularly true for the most massive ($\geq 15\ M_\odot$) O-type stars. While a growing number of B-type young stellar objects (YSOs) has recently been found to be associated with a disk/jet system (Beltrán & de Wit 2016), indicating a formation route similar to that of low-mass stars, the observation of disks around O-type YSOs remains elusive. The most luminous YSOs are sometimes found at the center of large (a few 10^3 au in size), massive ($\sim$10 $M_\odot$) cores showing well-defined velocity gradients, interpreted as gravitationally unstable, transient structures undergoing rotation and/or infall towards the central objects ("rotating toroids", Beltrán et al. 2005).

G24.78+0.08

The detection of radio jets and/or collimated molecular outflows from O-type YSOs is also rare, although this picture may change in the coming years thanks to sensitive surveys of outflows in high-mass star-forming regions (Moscadelli et al. 2016; Purser et al. 2016; Rosero et al. 2016). Single-dish and interferometric observations seem to indicate that early B-type stars show on average more collimated outflows than late O-type stars (see, e.g., Beuther & Shepherd 2005). This could point to an increasing outflow decollimation resulting from the larger stellar ionizing flux (Peters et al. 2011) and radiation pressure (Vaidya et al. 2011; Kuiper et al. 2016), and more powerful stellar wind of a more massive star. However, the less collimated outflows observed in more luminous regions could simply be an effect of the insufficient angular resolution, if a large number of unresolved YSOs contribute to the observed outflow pattern (Peters et al. 2014).

The gas kinematics around the most massive YSOs, in regions at relatively large distances (2–10 kpc), with high visual extinction and a high degree of clustering, can only be studied via high-angular ($\leq 1''$) resolution observations in less extinct bands (from radio to NIR). Recently, the Atacama Large Millimeter/submillimeter Array (ALMA), thanks to its superb sensitivity and sub-arcsecond angular resolution, has allowed a great advance in the detection of Keplerian disks towards B-type YSOs (Sánchez-Monge et al. 2013; Beltrán et al. 2014), and even provided evidence for disks around O-type stars (Johnston et al. 2015; Ilee et al. 2016). With this in mind, we have carried out an ALMA program during Cycle 2 observations to search for disks towards a selected sample of luminous ($>10^5\ L_\odot$) YSOs. The description of this project and the general findings of this study have recently been reported by Cesaroni et al. (2017). The present paper focuses on a specific target of the sample, the massive star-forming region G24.78+0.08.

The region of high-mass star formation G24.78+0.08, with bolometric luminosity of $\sim 2 \times 10^5\ L_\odot$ at a distance of 7.2 ± 1.4[1] kpc, has already been the target of high-angular-resolution studies using several interferometers, such as the

Plateau de Bure (PdBI), the Submillimeter Array (SMA) and the Very Large Array (VLA; Beltrán et al. 2006, 2007, 2011; Moscadelli et al. 2007). At scales of $\sim 10^4$ au, a necklace of six (sub)millimeter dusty cores is observed along the SE–NW direction, among which the most prominent ones are two cores, named A1 and A2, separated by only $1''\!.5$ and located at the center of the necklace (see Fig. 1). The kinematics of both cores is characterized by a SW–NE LSR velocity ($V_{\rm LSR}$) gradient (revealed in different lines of high-density tracers such as CH$_3$CN and its isotopologs), supporting the interpretation that the two cores are rotating toroids (Beltrán et al. 2006). Inside core A1, VLA A-Array (1.3 cm and 7 mm) observations have revealed an intense (~ 10 mJy beam^{-1} at 1.3 cm), hypercompact (HC) (size ≈ 1000 au) H II region. Beltrán et al. (2006) mapped the core with the VLA B-Array in NH$_3$ and detected red-shifted absorption towards the HC H II region, suggesting mass infall on scales of 5000 au. At smaller scales, multi-epoch VLBI observations have detected an arc-like distribution of 22 GHz water masers delimiting the HC H II region to the N and NE, and have measured high (≥ 40 km s^{-1}) velocities of the masers expanding away from the center of the HC H II region (Moscadelli et al. 2007).

Intense 6.7 GHz CH$_3$OH and 22 GHz H$_2$O maser emissions are commonly found near massive YSOs, and, observed with Very Long Baseline Interferometry (VLBI), are useful probes of the gas three-dimensional (3D) kinematics. In particular, while the 6.7 GHz CH$_3$OH masers generally trace slow rotation and/or expansion of the disk/envelope of the massive YSO (Sanna et al. 2010b; Moscadelli et al. 2011; Moscadelli & Goddi 2014), water masers emerge from shocked molecular gas at the interface between fast flows and the ambient material, thus efficiently tracing the structure of (proto)stellar outflows close to (within 10–100 au of) the massive YSO (Goddi et al. 2005; Goddi & Moscadelli 2006; Moscadelli et al. 2007, 2011, 2013; Sanna et al. 2010b, 2012).

For all this, the combination of ALMA thermal and VLBI maser observations is presently the most accurate technique to infer the physical conditions and study the motion of the gas very close to OB-type YSOs. This article presents an application of this technique towards the O-type YSO exciting the HC H II region in the G24.78+0.08 A1 molecular core. Section 2

describes the new ALMA, VLBI, and *Jansky* Very Large Array (JVLA) observations. The method of analysis of the ALMA data is presented in Sect. 3. The main observational results are shown in Sect. 4. In Sect. 5, we analyze the mass and 3D velocity distribution inside core A1, and discuss its dynamical state and the excitation conditions of the gas. The main findings are summarized in Sect. 6.

2. Observations and data calibration

2.1. ALMA

G24.78+0.08 is one of the six targets of the program "2013.1.00489.S" to search for disks around O-type YSOs, observed by ALMA during Cycle 2 in July and September 2015. A full description of the ALMA observations, correlator setup, data calibration and imaging is given in Cesaroni et al. (2017). Here we recall only a few general observational parameters and information specific to the G24.78+0.08 dataset. The systemic velocity of G24.78+0.08, employed for Doppler correction during observations, was $V_{sys} = 111.0$ km s^{-1}. Thirteen spectral windows (SPW) were observed over the frequency range 216.0–237 GHz, one broad (bandwidth of 1.9 GHz) SPW, for sensitive continuum measurement, and twelve narrow (0.23 GHz) SPWs, to achieve high-velocity resolution (0.33–0.66 km s^{-1}) for the targeted spectral lines. Data calibration was performed using the pipeline for ALMA data analysis in the Common Astronomy Software Applications (CASA, McMullin et al. 2007) package, version 4.4. The images for the continuum and line emissions were produced manually using the CLEAN task, with the robust parameter of Briggs (1995) set to 0.5, as a compromise between resolution and sensitivity to extended emission. The full width at half maximum (FWHM) clean beam of the resulting images is about 0″.2. The accuracy in the absolute position of the ALMA images is expected to be ~50 mas. The continuum image of G24.78+0.08 has a 1σ rms noise level of 1.0 mJy beam^{-1}, limited by the dynamic range. The 1σ rms noise in a single spectral channel varies in the interval 1–2 mJy beam^{-1}, depending on the considered SPW.

We have developed a specific procedure to determine the continuum level of the spectra and subtract it from the line emission. Since in G24.78+0.08 (as well as in the other targets of our ALMA program) almost all the observed SPWs present a "line forest", identifying the channels where no line emission is present is a very difficult task. For each SPW, we use STATCONT[2] (Sanchez-Monge et al. 2017), a statistical method to estimate the continuum level at each position of the map from the spectral distribution of the intensity at that position. The validity of our procedure is described in detail and tested with numerical simulations by Sanchez-Monge et al. (2017).

2.2. EVN: 6.7 GHz CH₃OH masers

We observed G24.78+0.08 (tracking center: RA (J2000) = 18^{h}36^{m}12^s.55 and Dec (J2000) = −07°12′ 10″.9) with the European VLBI Network[3] (EVN) in the $5_1 - 6_0$ A^+ CH₃OH transition (rest frequency 6.668519 GHz). Data were taken at three epochs: 2007, March 20 (program code: EM064B), 2009, March 12 (EM064F), and 2012, November 3 (EM099B). The antennae involved in the observations were Jodrell2, Effelsberg, Medicina, Noto, Torun, Westerbork, Cambridge

(epochs 1 and 2, only), Onsala (epochs 2 and 3), Hartebeesthoek (epoch 1), and Yebes (epoch 3). During runs of 6–7 h, we recorded dual circular polarization through eight adjacent bandwidths of 2 MHz, one of them centered at the maser V_{LSR} of 110.0 km s^{-1}. The eight 2 MHz bandwidths were used to increase the signal-to-noise ratio (S/N) of the weak continuum (phasereference) calibrator. The data were processed with the MKIV correlator at the Joint Institute for VLBI in Europe (JIVE, at Dwingeloo, the Netherlands) in two correlation passes, using 1024 and 128 spectral channels to correlate the maser 2 MHz bandwidth and the whole set of eight 2 MHz bandwidths, respectively. The spectral resolution attained across the maser 2 MHz band was 0.09 km s^{-1}. In each correlator pass, the data averaging time was 1 s.

In order to determine the maser absolute positions, we performed phase-referencing observations in fast switching mode (cycle intervals of 4–5 min) between the maser source and the calibrator J1825−0737 (intensity ≈0.4 Jy beam^{-1} at 6 GHz, target separation ≈2.7°, position uncertainty ±1.0 mas). Data were reduced with AIPS following the VLBI spectral line procedures (see, for instance, Sanna et al. (2010a) for a detailed description of the data calibration and analysis). The emission of an intense and compact maser channel was self-calibrated, and the derived (amplitude & phase) corrections were applied to all the maser channels before imaging. Reflecting the variation in the antennae taking part in the observations, the naturally weighted beam (excluding Hartebeesthoek) of the maser images slightly changes from epoch to epoch. The FWHM major and minor sizes of the beam range over 9–12 mas and 4–6 mas, respectively, and the beam PA varies from −33° to +30°. In channel maps with (relatively) weak signal, the 1σ rms noise is 6–7 mJy beam^{-1}, close to the expected thermal noise. Table B.1 reports the parameters (intensity, V_{LSR}, position and proper motion) of the 6.7 GHz methanol masers in the G24.78+0.08 A1 core. Proper motions are relative to the geometric center (hereafter "center of motion", identified with label #0-A1N in Table B.1) of the maser features belonging to the cluster A1N associated with the HC HII region (see Sect. 4). The center of motion is calculated selecting features with stable spatial and spectral structure, persisting over the three observing epochs. The more the maser kinematics is symmetrical with respect to the star ionizing the HII region, the more the "center of motion" approximates the reference system comoving with this star.

2.3. Jansky Very Large Array

G24.78+0.08 was observed using the JVLA of the National Radio Astronomy Observatory (NRAO)[4] in A configuration (project code: 15A-019) employing five two-hour runs: on June 23, June 26, July 05, August 18, September 23 2015. We used the 1.3 cm (K-band) receiver and the WIDAR correlator to simultaneously record a wide (≈3 GHz, dual polarization) bandwidth for the continuum emission and a set of narrow (8 and 16 MHz) bandwidths centered on NH₃ inversion and hydrogen recombination lines. This article reports on only the 1.3 cm continuum observations, the NH₃ and hydrogen recombination lines being the subject of a future paper. Depending on the LST range of the run, the primary flux calibrator was either 3C286 or 3C48; the phase-calibrator was the compact ("P" code), strong (bootstrapped flux ≈1 Jy), and nearby (target separation ≈3.5°) quasar J1832−1035.

---

[2] http://www.astro.uni-koeln.de/~sanchez/statcont
[3] The European VLBI Network is a joint facility of independent European, African, Asian, and North American radio astronomy institutes.

[4] NRAO is a facility of the National Science Foundation operated under cooperative agreement with Associated Universities, Inc.

Several scans were missed in the second observing run (June 26), and we do not use this subset of data. The analysis of the remaining four runs was performed in CASA, employing the standard VLA calibration pipeline.[5] We carefully inspected the pipeline results, and after flagging a small fraction of more scattered data, we reran the pipeline again. After applying the calibration, the continuum uv-data of the four runs were merged together, and averaged in frequency. Taking advantage of the intense flux ($\approx$16 mJy), we self-calibrated the continuum uv-data, gaining a factor $\approx$2 in the S/N of the final image. Using "Briggs" weighting with robust 0, the restoring beam is $0\rlap{.}''093 \times 0\rlap{.}''079$ at PA = 19.6°. The expected accuracy in the absolute position of the continuum image is ~20 mas. The rms noise on the final image is 14 μJy beam^{-1}.

3. Data analysis

The molecular emission emerging from high-mass star-forming regions is typically very complex (see, for instance, Cesaroni et al. 2017, Fig. 5). Each of the observed spectral windows towards G24.78+0.08 contains a multitude of lines from different molecular species which makes it very difficult to both (1) select emission-free channels and (2) unambiguously identify the transitions of a given molecule. Concerning point (1), we have used the STATCONT tool (see Sect. 2.1). Regarding point (2), a robust way of molecular identification is through the simultaneous fit of multiple transitions of a given molecular species. For this purpose, we use the XCLASS (eXtended CASA Line Analysis Software Suite) tool (Möller et al. 2017). This tool models the data by solving the radiative transfer equation for an isothermal homogeneous object in local thermodynamic equilibrium (LTE) in one dimension. The finite source size, dust attenuation, and line opacity are considered as well.

The first step of our analysis was inspecting the spectral emission of G24.78+0.08 A1 to identify, with the guidance of XCLASS synthetic spectra, the molecular species showing a relatively high number of (almost) unblended lines. Table 1 lists the chosen molecules (in boldface characters) and the corresponding transitions. Since we wish to exploit the data to study the physical conditions and kinematics of the region with the highest possible detail, we consider only molecules of low/moderate optical thickness.[6] Four (CH$_3$OCHO, ^{13}CH$_3$CN, ^{13}CH$_3$OH and CH$_3$CH$_2$CN) out of the five selected molecules present (unblended) transitions of comparable level energies, 30 K $\leq E_u/k \leq$ 320 K, with CH$_3$OCHO showing the highest number of lines and being the most reliable tracer of moderately warm gas (see the recent work by Rivilla et al. 2017a). The transitions of vibrationally excited CH$_3$CN have significantly higher level energies, 590 K $\leq E_u/k \leq$ 780 K, and are suitable to trace the conditions of warmer gas (assuming that LTE holds).

Subsequently, we employed XCLASS to produce maps of column density, temperature, velocity and line width of the G24.78+0.08 A1 region, by extracting spectra pixel-by-pixel from the images of the SPWs and fitting all the unblended lines of a given molecular species simultaneously. The explored parameter space was: 10^{13} cm^{-2} $\leq N_{tot} \leq 10^{19}$ cm^{-2} for the column density; $|V_{LSR} - V_{sys}| \leq 8.0$ km s^{-1}, for the offset in V_{LSR} from the systemic velocity; 0 km s^{-1} $\leq FWHM \leq$ 12 km s^{-1}, for

the line width; 50 K $\leq T_{rot} \leq$ 400 K and 100 K $\leq T_{rot} \leq$ 700 K, for the rotational temperature of the four molecules with low-energy transitions and vibrationally excited CH$_3$CN, respectively. Figures 2 and 3 show examples of spectra and the corresponding XCLASS fits to all the selected unblended transitions, for a map pixel (located in between the A1N and A1M regions – see Fig. 5) well representing the average quality of satisfactory fits. One can note that, in almost all cases, the profile of the selected lines is relatively well reproduced. The maps derived from fits to the CH$_3$OCHO transitions are those of the highest quality, that is, the smoothest ones and those without bad-fit pixels (within the region of sufficiently intense CH$_3$OCHO emission where the maps are determined – see Fig. 5). The maps obtained from the ^{13}CH$_3$CN and vibrationally excited CH$_3$CN lines are still of good quality over most of the fitted region (see Figs. 6 and 7). Instead, the maps produced by fitting the ^{13}CH$_3$OH and CH$_3$CH$_2$CN emission are more irregular and appear to be unreliable in large portions of the fitted area. The main reason for the low-quality fits is significant line blending for ^{13}CH$_3$OH and (relatively) low S/N for CH$_3$CH$_2$CN. Since, where the fit has acceptable quality, the maps from ^{13}CH$_3$OH and CH$_3$CH$_2$CN are qualitatively similar to the maps from CH$_3$OCHO, ^{13}CH$_3$CN, and vibrationally excited CH$_3$CN, in the following we present and discuss only the maps of these three latter molecular species.

In addition to the molecular transitions fitted with XCLASS, in our analysis (see Sects. 4, 5.3 and 5.4) we have employed the H30α and SO$_2$ 16$_{1,15}$–15$_{2,14}$ lines, as well. The corresponding frequencies and energies are listed at the bottom of Table 1. Both emissions are intense (see Figs. 8 and 3) and not significantly contaminated by other molecular lines. More specifically, there are two lines of CH$_3$OCHO close in frequency to the H30α line, but, by fitting their spectral profiles, we have ascertained that their contamination is only 10–30% of the total emission and is confined to two frequency intervals (1.5 MHz wide) that are very small compared with the H30α line width ($\approx$40 MHz – see Fig. 8, upper panel).

4. Results

4.1. Continuum emission

Figure 4 shows that the ALMA 1.4 mm and JVLA 1.3 cm continua present similar spatial distributions, both being dominated by intense and compact emission from the HC H II region N of core A1. In the following, we refer to this area as A1N. The (spatially integrated) continuum spectrum can be fitted with a simple model accounting for optically thin free-free emission from a homogeneous H II region with electron temperature 10^4 K, radius 1100 au, and Lyman continuum luminosity of the ionizing star of 7.2×10^{47} s^{-1}. Thus the contribution of the dust emission to the integrated flux of the HC H II region appears to be negligible even at 1.4 mm. The small offset in position between the peaks of the two continuum images (the 1.4 mm peak is offset $\approx$50 mas to SW with respect to the 1.3 cm peak) is within the combined (ALMA plus JVLA) absolute position uncertainty, and is probably not significant. The spur/tail of weaker emission have different orientations, directed towards SW and S at 1.3 cm and 1.4 mm, respectively.

4.2. Density, temperature, and V_{LSR} distribution

Figures 5, 6, and 7 present the maps of column density, rotational temperature, V_{LSR} and line width towards the core A1, obtained

---

[5] For details, see https://science.nrao.edu/facilities/vla/data-processing/pipeline/scripted-pipeline
[6] The optical depths, average over core A1, of the transitions fitted with XCLASS are: for CH$_3$OCHO $\lesssim$ 0.1, for ^{13}CH$_3$CN $\lesssim$ 0.2, for CH$_3$CN v$_8$ = 1 $\lesssim$ 0.3, and for ^{13}CH$_3$OH $\lesssim$ 0.1.
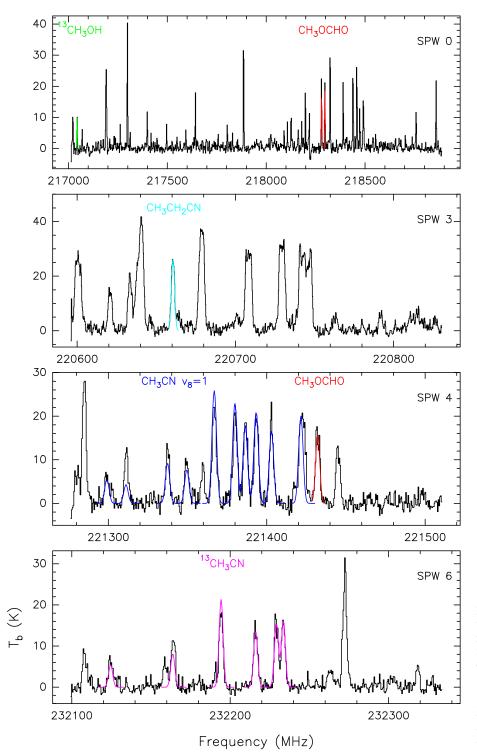
Fig. 2. XCLASS fit of the selected molecular transitions in the SPWs 0, 3, 4 and 6. Each panel refers to a different spectral window, indicated in the upper-right corner. The observed spectra, extracted from a single pixel of the maps, are shown in black, while the spectral fits to the chosen emission lines are in colors. Different colors are used to distinguish the transitions of distinct molecular species, as indicated at the top of the panels. The spectra are shown in brightness temperature versus rest frequency.

by fitting simultaneously with XCLASS multiple transitions (see Table 1) of CH_3OCHO, vibrationally excited CH_3CN and $^{13}CH_3CN$. Comparing the maps, it is evident that the V_{LSR} and line-width maps obtained from fits to these three different molecular species are well consistent. On the one hand, this confirms our expectation that, being optically thin, the three molecules trace the same portion of the gas; on the other hand, it supports the reliability of our results. The V_{LSR} maps present a clear gradient directed approximately from S (blueshifted) to N (redshifted). The most southern tip of the

core A1 emits at $V_{LSR} \approx 106$ km s^{-1}, the central region is at $V_{LSR} \approx 109$ km s^{-1}, and the region A1N has an average $V_{LSR} \approx 113$ km s^{-1}. The methanol maser emission concentrates in two main clusters: 1) around the HC HII region in A1N; and 2) in an E–W linear distribution ($\approx 0\rlap{.}{''}25$ in extent, labeled A1SW in Figs. 5, 6 and 7, upper-left panels) at the SW tip of the core A1. The good V_{LSR} correspondence between the methanol masers and the three different molecular species indicates that the maser and thermal lines trace the same kinematics. The only notable exception are a few maser spots detached from the center of the
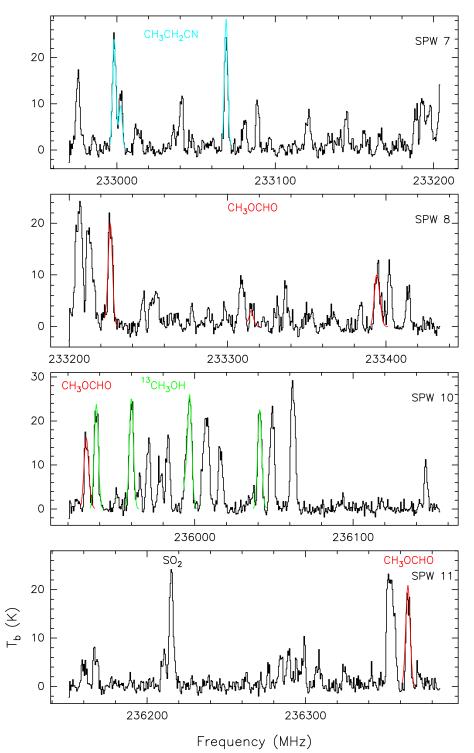
Fig. 3. As in Fig. 2 for the SPWs 7, 8, 10 and 11. The SO_2 line is labeled in the SPW 11.

HC HII region and projected on top of the SW tail of the 1.3 cm continuum, most of which have V_{LSR} significantly lower than that of the molecular lines (at the same position).

The maps of line widths of the three molecular species are remarkably similar. In each of the three maps, the measured line widths vary in the interval 2–9 km s^{-1}, and are larger than 6 km s^{-1} over the same region, extending $\approx 0''3$ N–S between A1N and A1SW. Within this region, two areas of significantly wider line widths (up to $\approx$8–9 km s^{-1}) are notable (see Figs. 5, 6 and 7, lower-right panels): 1) to the N, a compact spot SW of the radio continuum peak, which we name LW-CS;

and 2) to the S, an elongated ridge, located between the tail of the 1.3 cm continuum emission and the methanol maser cluster A1SW, named LW-ER.

When comparing density and temperature maps obtained from different molecular species, one must bear in mind that differences in the map distributions can naturally result from several factors, among which varying excitation conditions, chemical segregation and non-LTE effects are probably the most important. Despite this, the maps of column density of CH_3OCHO, vibrationally excited CH_3CN, and $^{13}CH_3CN$ are in reasonable agreement throughout the whole core A1. The peak

Table 1. List of the molecular transitions considered in this work.

Mol. Species	Frequency (MHz)	Resolved QNs	E_u/k (K)
CH$_3$OCHO	218280.900	$17_{3,14}-16_{3,13}$ E	100
	218297.890	$17_{3,14}-16_{3,13}$ A	100
	221433.019	$18_{11,7}-17_{11,6}$ A	181
	233226.788	$19_{4,16}-18_{4,15}$ A	123
	233315.780	$19_{15,4}-18_{15,3}$ E	261
	233394.655	$19_{14,6}-18_{14,5}$ A	242
	233396.680	$19_{14,5}-18_{14,4}$ E	242
	235932.379	$19_{7,12}-18_{7,11}$ A	145
	236365.574	$20_{3,18}-19_{3,17}$ A	128
CH$_3$CN v$_8$=1	221299.495	$J_K = 12_{-4}-11_{-4}$	762
	221311.835	$J_K = 12_6-11_6$	771
	221337.928	$J_K = 12_{-3}-11_{-3}$	698
	221350.257	$J_K = 12_5-11_5$	706
	221367.404	$J_K = 12_{-2}-11_{-2}$	649
	221380.595	$J_K = 12_4-11_4$	655
	221387.233	$J_K = 12_{-1}-11_{-1}$	615
	221394.056	$J_{lK} = 12_0-11_0$	594
	221403.511	$J_K = 12_3-11_3$	619
	221422.342	$J_K = 12_2-11_2$	596
^{13}**CH$_3$CN**	232125.130	$J_K = 13_5-12_5$	257
	232164.369	$J_K = 13_4-12_4$	193
	232194.906	$J_K = 13_3-12_3$	142
	232216.726	$J_K = 13_2-12_2$	107
	232229.822	$J_K = 13_1-12_1$	85
	232234.188	$J_K = 13_0-12_0$	78
^{13}**CH$_3$OH**	217044.616	$14_{1,13}-13_{2,12}$	254
	235938.220	$5_{-1,5}-4_{-1,4}$	40
	235960.370	$5_{0,5}-4_{0,4}$	34
	235997.230	$5_{3,3}-4_{3,2}$	84
	236041.400	$5_{1,4}-4_{1,3}$	55
CH$_3$CH$_2$CN	220660.918	$25_{2,24}-24_{2,23}$	143
	232998.740	$26_{8,19}-25_{8,18}$	222
	233002.700	$26_{12,15}-25_{12,14}$	311
	233069.379	$26_{7,19}-25_{7,18}$	205
H30α	231900.928		
SO$_2$	236216.687	$16_{1,15}-15_{2,14}$	131

Notes. Transitions of the molecules given in boldface characters have been fitted with XCLASS (see Sect. 3).

in column density of the three molecular species falls inside a common area (indicated with A1M in Figs. 5, 6 and 7, upper-left panels) located $\approx0.''4$ (or 2900 au) S of the radio continuum peak in A1N. In the maps of CH$_3$OCHO and ^{13}CH$_3$CN, a less prominent but significant enhancement in molecular column density (up to a value about half of the map maximum) is also observed at a location (labeled A1N-W) at the western border of the HC H II region. In good positional correspondence with this density enhancement in A1N-W, the maps of rotational temperature of all the three molecular species (see Figs. 5, 6 and 7, upper-right panels) consistently show a plateau of relatively high gas temperatures, 300–400 K. However, the rotational temperature maps of the three molecular species present clear differences,
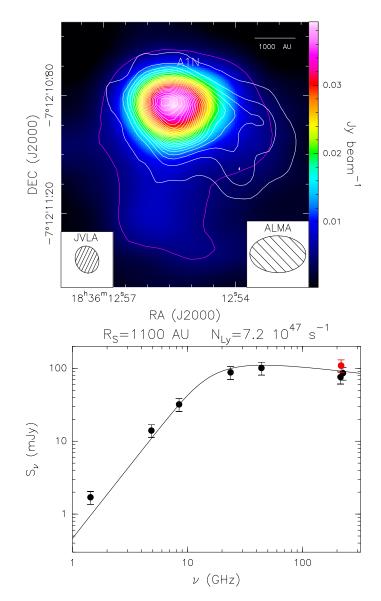

Fig. 4. *Upper panel*: the color map represents the ALMA 1.4 mm continuum, with the color-intensity scale shown in the wedge on the right of the panel. The magenta contour is the 5σ threshold of 5 mJy beam^{-1}. The white contours reproduce the JVLA A-Array 1.3 cm continuum, plotting levels from 0.1 to 16, by 0.7 mJy beam^{-1}. The insets in the right and left bottom corners of the plot report the ALMA and JVLA beams, respectively. *Lower panel*: spectrum (black error bars) and fit (black curve) of the continuum emission over the frequency range 1.4–225 GHz. The fluxes at 1.4, 4.9, and 8.4 GHz are from VLA observations not yet published (Cesaroni, private communication); fluxes at 24, 44, 214, and 225 GHz come from VLA B-Array (Beltrán et al. 2006), VLA A-Array (Beltrán et al. 2007), PdbI, and SMA (Beltrán et al. 2011) observations, respectively. We have fitted the continuum spectrum with a simple model of a spherical, homogeneous H II region: the derived radius and Lyman photon flux are reported at the top of the panel. The red error bar gives the ALMA 1.4 mm flux integrated over the H II region (delimited by the weakest white contour in the upper panel).

too. While the rotational temperature of vibrationally excited CH$_3$CN is high, $\geq$220 K, only towards the HC H II region in A1N, the temperature of CH$_3$OCHO and ^{13}CH$_3$CN reach high values, up to 300–400 K, towards A1M as well. As discussed more in detail in Sect. 5.6, the lower rotational temperatures derived for the vibrationally excited transitions of CH$_3$CN in A1M are probably due to their much higher level energies
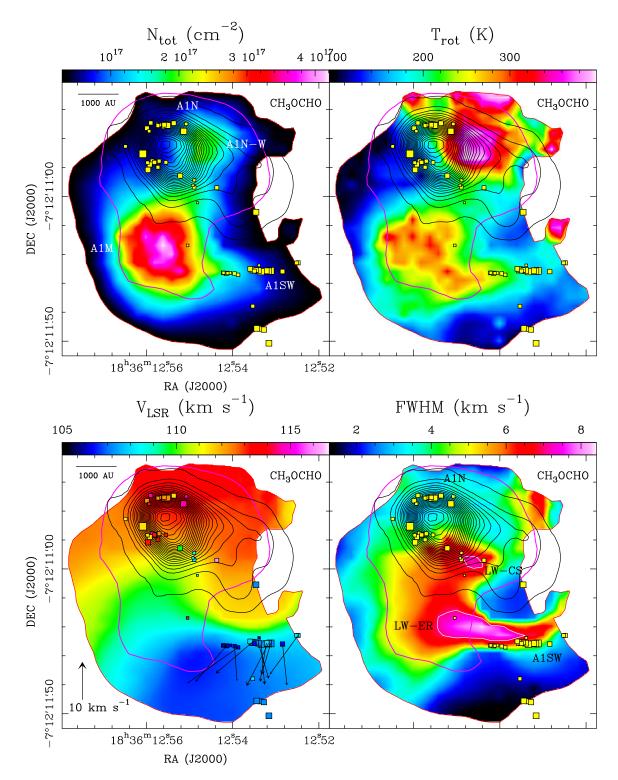
Fig. 5. Results from simultaneously fitting the emission of nine unblended transitions of CH_3OCHO with XCLASS (see Table 1 and Sect. 3 for details). *Upper panels*: maps of column density (*left*) and rotational temperature (*right*). *Lower panels*: maps of V_{LSR} (*left*) and line width (*right*). The maps are shown inside the region of core A1 where the column density of CH_3OCHO is higher than 3×10^{16} cm^{-2} (red contour). The magenta contour is the 5σ threshold of the ALMA 1.4 mm continuum emission. The black contours reproduce the JVLA A-Array 1.3 cm continuum (plotting the same levels as in the upper panel of Fig. 4). We label with "A1N", "A1N-W", "A1M" and "A1SW" four regions of interest of the core A1. In the FWHM map, the two white contours correspond to a level of *FWHM* = 7 km s^{-1}, and delimite the two regions of prominent line widths LW-CS (to the N) and LW-ER (to the S). The yellow squares give the absolute positions of the 6.7 GHz CH_3OH masers, determined via multi-epoch, sensitive EVN observations. Square area scales with the maser intensity. After correcting for the apparent motion between the EVN and ALMA observations, maser absolute positions are accurate within a few milliarcsecs. In the V_{LSR} map, 6.7 GHz masers are represented with colored squares to recognize their V_{LSR}, and black arrows show the proper motions of the masers in the cluster A1SW with respect to the barycenter of the masers in the cluster A1N (see Table B.1). The amplitude scale for proper motion is shown in the lower-left corner of the plot.
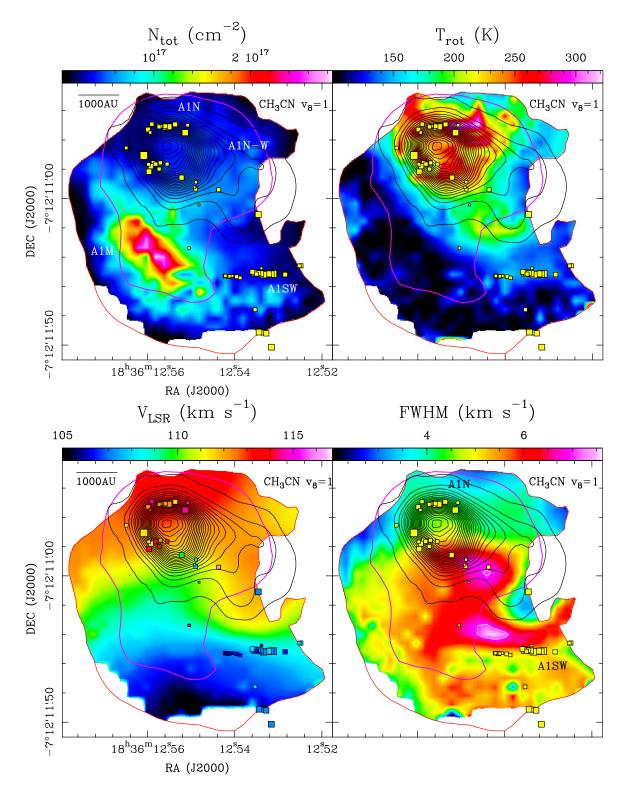
Fig. 6. As in Fig. 5, but for ten unblended, vibrationally excited transitions of CH$_3$CN (see Table 1 and Sect. 3 for details). The southern portion of the maps has been masked, because the fit quality is not satisfactory.

(590–780 K) and peculiar (radiative) excitation conditions. On the contrary, the fitted transitions of CH$_3$OCHO and ^{13}CH$_3$CN have level energies (70–260 K) comparable with the kinetic temperatures expected over core A1, and should be collisionally excited and, therefore, suitable tracers of the gas temperature. Between these two latter molecular species, the temperatures determined using CH$_3$OCHO, by fitting a larger number

of transitions optically thinner than those of ^{13}CH$_3$CN, are expected to be the more reliable ones.

4.3. The V_{LSR} pattern in the H30α line

Figure 8 (upper panel) shows that intense and broad emission in the H30α line is observed towards the HC H$_{II}$ region in A1N.
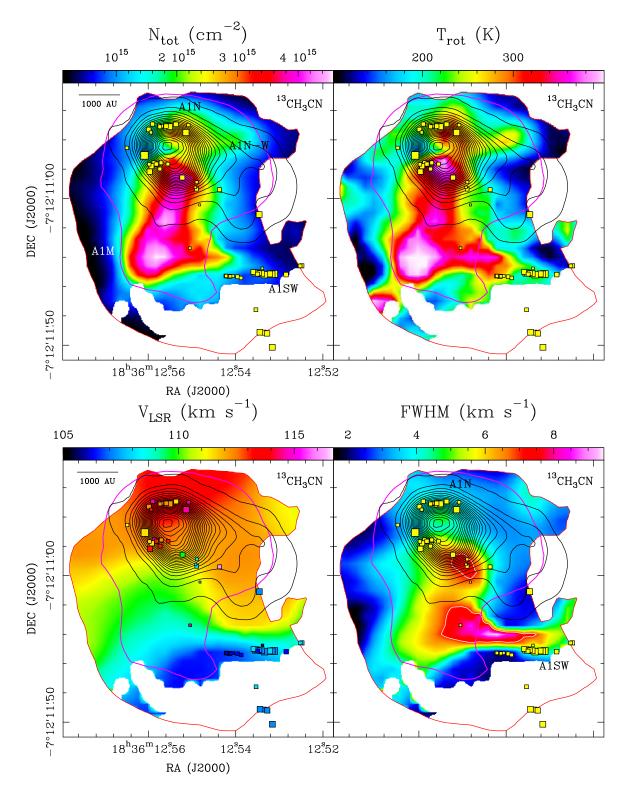
Fig. 7. As in Fig. 5, but for six unblended transitions of $^{13}CH_3CN$ (see Table 1 and Sect. 3 for details). The southern portion of the maps has been masked, because the fit quality is not satisfactory.

The angular resolution of our ALMA observations is not enough to resolve its spatial structure (see Fig. 8, central panel), but we can still probe the kinematics of the ionized gas by studying how the position of the compact emission peak changes in velocity. This is obtained by fitting the emission in the channel maps with a two-dimensional (2D) Gaussian. Figure 9 reveals that a well-defined V_{LSR} gradient is observed in the H30α line. It is directed at $PA = 39°$ (approximately parallel to the major axis of the VLA 7 mm continuum image) and extends over a relatively large velocity range, from ≈ 85 km s^{-1} to ≈ 139 km s^{-1} going from SW to NE. The velocity gradient, 22 km s^{-1} mpc^{-1} (see Fig. 8, lower panel), is one of the highest so far observed towards HC HII regions. In W51e2, probably the HC-HII region with the most accurate measurement of
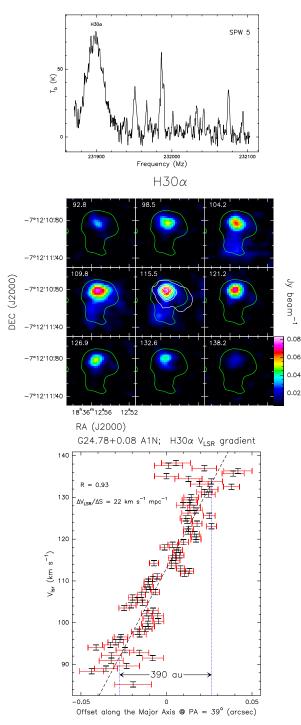
Fig. 8. *Upper panel*: spectrum of the SPW 5 in correspondence with the continuum peak in A1N. The strong and wide H30α line is labeled. *Central panel*: channel maps at different velocities across the H30α line width, showing the compact structure of the emission. The more diffuse emission is mostly due to two weak CH$_3$OCHO lines. In all panels, the green contour is the 5σ threshold (5 mJy beam^{-1}) of the ALMA 1.4 mm continuum. In the central panel, the white contours reproduce the JVLA A-Array 1.3 cm continuum, plotting levels from 0.1 to 16, by 3 mJy beam^{-1}. *Lower panel*: plot of channel V_{LSR} vs. corresponding peak positions, projected along the major axis of the peak distribution at PA = 39°. Black vertical error bars are equal to the channel width of 0.6 km s^{-1}; red horizontal error bars give the peak position errors, estimated with the expression (Reid et al. 1988): $(\Theta/2)(\sigma/I)$, where Θ is the FWHM size of the observing beam, and I and σ are the peak intensity and the channel rms noise, respectively. The dashed line is a linear fit to the data. A lower limit to the size of the region harboring the V_{LSR} gradient is indicated.

the velocity distribution of the ionized gas from previous works, Keto & Klaassen (2008) observe a V_{LSR} gradient of ≈ 0.5 km s^{-1} mpc^{-1}. This is approximately 40 times less than the value determined for the HC HII region in G24.78+0.08. The origin of such a large V_{LSR} gradient in the ionized gas is discussed in Sects. 5.3 and 5.5.

4.4. Three-dimensional motion of the methanol and water masers

In G24.78+0.08 A1N, the interaction of the HC HII region with the surrounding molecular environment can be traced with both water and methanol masers. While water masers trace dense neutral gas at the border of the ionized gas, methanol masers are observed at relatively larger separation from the center of the HC HII region (see Fig. 9). Figure 10 shows the 3D velocities of the two maser species, derived via multi-epoch VLBI observations. The water maser proper motions have already been presented in Moscadelli et al. (2007). They witness the fast (≈ 40 km s^{-1}) expansion of dense circumstellar gas towards N and E of the HC HII region. Based on sensitive, multi-epoch EVN observations, we present, for the first time, the proper motions of the 6.7 GHz methanol masers in G24.78+0.08. Methanol masers are observed to the N, SE and S of the HC HII region. SW of the 7 mm continuum peak, along the axis of the cometary-shaped, radio continuum emission, no water masers and only a few weak methanol masers are detected. Methanol masers move at significantly lower velocities (mainly ≤ 10 km s^{-1}) than the water masers. The methanol masers to the N draw an E–W line (as do the water masers observed at similar PA from the star but at smaller radii) and share a common motion towards NW. The proper motions of the methanol masers distributed to SE and S of the HC HII region are less ordered, but most of them indicate an expanding motion from the ionized gas.

5. Discussion

5.1. Molecular mass distribution inside core A1

We wish to determine the distribution of molecular gas over core A1. Firstly, we separate the free-free and dust contribution in the 1.4 mm continuum from the HC HII region in A1N. The spectrum of the HC HII region presented in Fig. 4 shows that the extrapolation of the integrated flux at 44 GHz (101 mJy) in the optically thin regime can account for the peak emission, 86 mJy beam^{-1} (toward the HC HII region), at 225 GHz from previous SMA observations (Beltrán et al. 2011). The SMA beam in the very-extended configuration had a FWHM size of $\approx 0''5$, big enough to cover most of the area of the ionized gas. The latter is well represented by the region delineated by the weakest contour of the JVLA 1.3 cm continuum plotted in Fig. 4, and has a maximum NE–SW extension of $\approx 0''6$. Integrating the 1.4 mm ALMA continuum over this region, we derive a flux of 109 mJy (shown as a red error bar in Fig. 4, upper panel), higher than the previous SMA peak flux. Since the optically thin extrapolation of the 44 GHz flux corresponds to the minimum free-free continuum flux expected at 1.4 mm, the flux of dust seen in projection over the HC HII region must be less than 109 mJy − 86 mJy = 23 mJy.

The 1.4 mm ALMA flux integrated over core A1, 160 mJy, is in reasonable agreement with the corresponding flux, 187 mJy, derived from previous SMA observations (Beltrán et al. 2011). This indicates that the ALMA observations recover most of the flux on scales <1'' and are adequate to determine the mass
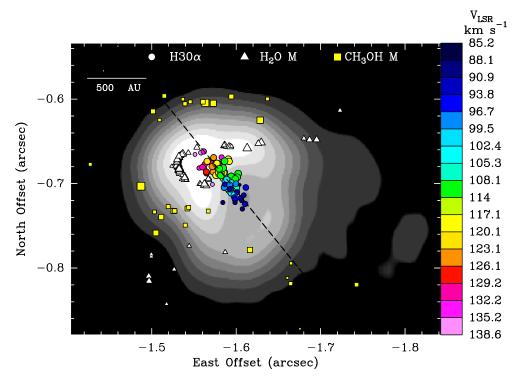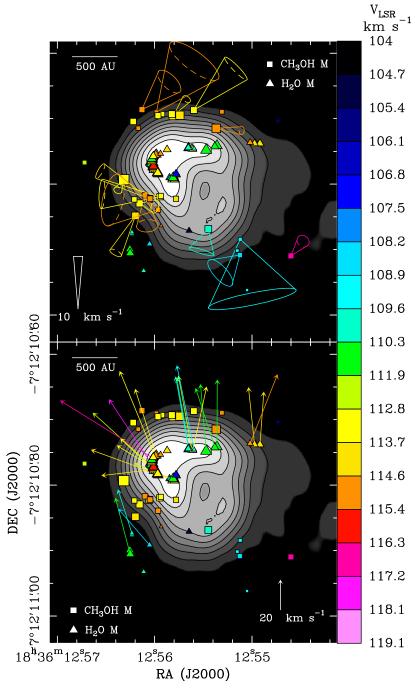
Fig. 9. Gray-scale image: VLA A-Array 7 mm continuum observed by Beltrán et al. (2007). The white triangles and yellow squares mark the VLBI positions of the H_2O 22 GHz and CH_3OH 6.7 GHz masers, with symbol area proportional to the logarithm of the maser intensity. The colored dots give the channel peak positions of the H30α line emission, with colors denoting V_{LSR} as indicated in the wedge on the right of the plot. The dashed black line marks the axis of the spatial distribution of the H30α peaks. The VLBI maser and VLA continuum absolute positions have been corrected for the apparent motion between the corresponding observing epochs and the ALMA observations, and should be accurate within 10 mas. The H30α position has been offset by 10 mas (less than the expected ALMA position accuracy) both to E and S, to obtain a better alignment with the axis of the radio continuum emission.

distribution inside core A1. The small difference between the ALMA and SMA fluxes can be ascribed to the shorter base-lines of the SMA observations, which can recover some of the more extended ($\gtrsim$ a few arcsec) emission. The flux of the 1.4 mm continuum over core A1 outside the HC HII region is 160 mJy − 109 mJy = 51 mJy. Thus, the total 1.4 mm flux from dust inside core A1 must lie in the range 51–74 mJy, where the upper limit is obtained adding to 51 mJy the maximum expected flux, 23 mJy, from dust over the area of the HC HII region. Assuming a dust opacity of 1 cm^2 g^{-1} at 1.4 mm (Ossenkopf & Henning 1994), a gas-to-dust mass ratio of 100, and a dust temperature equal to the average $T_{rot} \approx 200$ K (calculated from the map of CH_3OCHO T_{rot} – see Fig. 5, upper-right panel), we derive a total mass of molecular gas in core A1 of 4–7 $M_\odot$. From the aforementioned, dust flux upper limit, 23 mJy, the mass of molecular gas over the area of the HC HII region is estimated to be ≤ 2 $M_\odot$.

If the abundance of a given molecule is constant over core A1, for optically thin molecular and dust emission, the molecular column density (N_{tot}) has to be proportional to the dust emission. We find that the integral of the N_{tot} map of CH_3OCHO (see Fig. 5, upper-left panel) over the HC HII region is about one third of the integral over the whole core A1. This is in excellent agreement with the ratio of the 1.4 mm continuum fluxes $23/74 = 0.31$ corresponding to the same areas of integration, after correcting for the expected (minimum) contribution of free-free emission. From this comparison we deduce that the mass of molecular gas seen in projection over the HC HII region should be ≈ 2 $M_\odot$, and the total molecular mass inside core A1 ≈ 7 $M_\odot$. The estimated abundance of CH_3OCHO

is $\approx 2 \times 10^{-7}$, in good agreement with the value recently derived by Rivilla et al. (2017b) towards the massive star-forming region W51. The good correspondence between the CH_3OCHO N_{tot} map and the dust continuum map allows us to use the former to estimate the molecular mass of specific regions of core A1, taking advantage of the higher S/N of the former compared with the latter. By integrating N_{tot} within a relatively weak contour, 2.2×10^{17} cm^{-2}, around the map peak, the total molecular mass of the region A1M (see Fig. 5, upper-left panel) is found to be ≈ 2 $M_\odot$. Inside the region A1SW containing the linear cluster of 6.7 GHz masers, no local maximum of the CH_3OCHO column density is found. By integrating over a circle of diameter $0.''2$ (approximately the FWHM of the synthesized beam of the ALMA observations) centered on the maser cluster, the derived total mass is ≈ 0.2 $M_\odot$.

5.2. Velocity distribution inside core A1 and dynamical equilibrium

Previous interferometric (PdBI and SMA) observations towards the core G24.78+0.08 A1 identified a SW–NE ($PA \approx 50°$) V_{LSR} gradient in different lines of CH_3CN (Beltrán et al. 2004, 2011). This velocity gradient was interpreted as the rotation of a large (and massive) toroid, possibly gravitationally unstable and providing the reservoir of gas for the formation of the high-mass YSO at the center of the HC HII region. With the new ALMA data, Figs. 5–7 (lower-left panels) show that the V_{LSR} gradient throughout core A1 mapped in different molecular lines is oriented S–N, and covers a V_{LSR} range, ≈ 106–114 km s^{-1}, larger than observed before, ≈ 109–112 km s^{-1}

Fig. 10. Three-dimensional motions of the methanol (*upper panel*) and water (*lower panel*) masers in G24.78+0.08 A1N. In both panels, the gray-scale image and black contours (10–90%, at step of 10% of the image peak of 11 mJy beam^{-1}) reproduce the VLA A-Array 7 mm continuum. Colored triangles and squares report the absolute positions (evaluated at the date 2003 September 4) of the 22 GHz water and 6.7 GHz methanol masers, respectively, with colors denoting V_{LSR} as coded in the wedge on the right of the plot. In the upper panel, the 3D velocities of the methanol masers are shown with cones, with opening angle representing the uncertainty in the direction of motion and base ellipticity proportional to the ratio of the velocity components on the plane of the sky and along the line of sight. The white cone in the left bottom corner of the panel gives the scale for the velocity amplitude. In the lower panel, the sky-plane velocities of the water masers are indicated with arrows. The white arrow at the right bottom shows the velocity scale.

(Beltrán et al. 2011). We think that these differences are due to the higher angular resolution and sensitivity of the ALMA observations, which, for the first time, allow us to properly resolve the internal structure and kinematics of the individual cores (with sizes $\leq 1''$) in G24.78+0.08. The last point is clearly demonstrated by the agreement between the V_{LSR} maps obtained with ALMA using thermal lines and with VLBI of methanol masers at milliarcsecond angular resolution (see Fig. 5, lower-left panel).

Interpreting a V_{LSR} gradient as evidence of rotation and assuming equilibrium between gravitational and centrifugal forces, a dynamical mass can be calculated using the expression $M_{dyn} = (\Delta V^2 R)/(4 (\sin i)^2 G)$, where ΔV is the variation in V_{LSR}, R the radius of rotation, i the inclination angle (with respect to the line of sight) of the rotation axis, and G the gravitational constant. From the ALMA observations of core A1, we have $\Delta V \approx 8$ km s^{-1} and $R \approx 0''.45$ (or 3300 au), and derive

$M_{dyn} \approx 60 / (\sin i)^2 M_{\odot}$. To evaluate the inclination angle i, we use the average 3D velocity of the 6.7 GHz masers in A1SW with respect to the 6.7 GHz masers in A1N. Since the maser emission extends over a significant fraction of core A1 with V_{LSR} values in agreement with those of the thermal (molecular) lines, we are confident that the 6.7 GHz masers are reliable tracers of the kinematics of the molecular gas. The 3D velocity of the maser cluster A1SW with respect to the cluster A1N is calculated averaging V_{LSR} and proper motions of 16 and 11 persistent maser features belonging to clusters A1N and A1SW, respectively (see Table B.1). The number of employed features is sufficiently high to ensure that the dominant relative motion of the two clusters can be adequately measured. Assuming that core A1 undergoes rigid rotation and that the plane of rotation intersects the plane of the sky along S–N (to account for the orientation of the V_{LSR} gradient traced with the ALMA observations), in Appendix A

we derive that the angular velocity vector has an amplitude of 18 ± 3 km s^{-1} arcsec^{-1} and forms an angle $i = 53° \pm 8°$ with the line of sight. From this value of i, we obtain $M_{\rm dyn} = 94 \pm 20$ $M_\odot$.

To assess if core A1 is in rotational equilibrium, one has to compare $M_{\rm dyn}$ with the total mass in core A1. From the ALMA observations, we have estimated a total molecular mass of ≈ 7 $M_\odot$. To this, we must add the total mass in stars and ionized gas. Intense free-free emission is observed only from core A1N, whose spectrum has been successfully modeled in terms of a compact H II region, optically thin at frequency ≥ 20 GHz (see Fig. 4, lower panel). Our model provides an estimate of the density, $\approx 3.3 \times 10^5$ cm^{-3}, and radius[7], ≈ 1100 au, of the H II region, from which a total mass of ionized gas of $\approx 5 \times 10^{-3}$ $M_\odot$ is derived. This is negligible compared to the molecular mass in core A1.

It is relatively easy to estimate a lower limit for the total stellar mass inside core A1. The modeled H II region has a Lyman continuum flux of 7.2×10^{47} s^{-1}, typical of a zero-age main sequence (ZAMS) star of spectral type O9.5, with mass of 20 $M_\odot$ and bolometric luminosity of 4×10^4 $L_\odot$ (see, for instance, Panagia 1973). The assumption that a single star is responsible for the Lyman continuum flux of the HC H II region corresponds to the case of minimum stellar mass. Thus, the total stellar mass inside core A1 must be ≥ 20 $M_\odot$.

Since the total molecular mass, ≈ 7 $M_\odot$, is lower than the minimum stellar mass, 20 $M_\odot$, the total mass in core A1 depends critically upon a reliable estimate of the total stellar mass. This is not an easy task, since the high optical-infrared (IR) extinction towards core A1 hampers the study of the population of low/intermediate-mass stars. To estimate an upper stellar-mass limit, we can simply consider the densest stellar clusters in our Galaxy, the "super star clusters", which reach (stellar) mass surface density up to 10^5 $M_\odot$ pc^{-2} (Tan et al. 2014, Fig.1). Since core A1 has a size ≤ 0.03 pc, we can expect a content in stellar mass ≤ 100 $M_\odot$. This upper limit is within the range of values, 74–114 $M_\odot$, allowed for the core dynamical mass $M_{\rm dyn}$. Therefore, on the basis of these arguments only, we cannot exclude that core A1 is massive enough to be in rotational equilibrium. However, in Sect. 5.4, by comparing the kinematics of the ionized and molecular gas, we interpret the S–N $V_{\rm LSR}$ gradient as expansion of the whole core, rather than gravitationally supported rotation.

5.3. A fast bipolar outflow through the HC H II region

Figure 9 shows that the ionized gas harbors a large, $\approx \pm 30$ km s^{-1}, $V_{\rm LSR}$ gradient along the direction at $PA = 39°$. The pattern of $V_{\rm LSR}$, monotonically increasing from SW to NE and centered at a velocity near $V_{\rm sys} \approx 111$ km s^{-1}, seems to be inconsistent with a champagne flow interpretation (Tenorio-Tagle 1979), for which we would expect $V_{\rm LSR}$ close to $V_{\rm sys}$ at one edge of the spatial distribution of the velocity peaks. Using conservative lower limits for $\Delta V \geq 42$ km s^{-1} and $R \geq 195$ au, the dynamical mass inferred from this $V_{\rm LSR}$ gradient is $M_{\rm dyn} = (\Delta V^2 R)/(4 (\sin i)^2 G) \geq 96$ $M_\odot$. The lower limit for the size, 390 au, of the region harboring the $V_{\rm LSR}$ gradient has been estimated from Fig. 8, lower panel, excluding the weakest peaks with more uncertain positions at both edges of the linear distribution. The derived dynamical mass is much larger than the mass of the ionizing star estimated from the radio and bolometric luminosity, and rules out the interpretation of the $V_{\rm LSR}$ pattern in terms of

rotation/infall. The simplest interpretation of the observed $V_{\rm LSR}$ gradient in the H30α line is in terms of a fast, bipolar ouflow blowing from the massive YSO, placed at the center of the H30α pattern and responsible for the gas ionization.

Comparing Figs. 9 and 10 (lower panel), one notes that fast-moving (≥ 40 km s^{-1}) water masers are found just ahead of the NE lobe of the H30α flow. This suggests that the ionized gas hits the surrounding molecular environment at high velocity and produces a layer of shocked, dense gas favorable for water maser emission. At high ambient densities, $n_{\rm H_2} \geq 10^7$ cm^{-3}, shocks are expected to be radiative and momentum-driven. Momentum conservation implies a maser shock velocity $V_{\rm sh} \approx V_{\rm ion} \sqrt{\rho_{\rm ion}/\rho_{\rm mol}}$ (see, for instance, Masson & Chernin 1993), where $V_{\rm ion}$ is the velocity of the ionized flow, and $\rho_{\rm ion}$ and $\rho_{\rm mol}$ are the densities of the ionized and molecular gas, respectively. Since our model of the H II region predicts that the ionized gas is at least a factor ≈ 30 less dense than the surrounding molecular gas and the masers move close to the plane of the sky at average velocities of about 40 km s^{-1}, the ionized gas must reach velocities ≥ 200 km s^{-1}close to the plane of the sky. Considering that the most red-shifted $V_{\rm LSR}$ of the H30α flow observed in proximity of the water masers (see Fig. 9) implies a maximum line of sight velocity of only ≈ 30 km s^{-1}, we can infer that the axis of the ionized flow forms an angle $\leq 10°$ with the plane of the sky (pointing away from us towards NE). Comparing the orientation of the flow axis, at PA = 39°, with the angular distribution of the water maser proper motions, regularly varying over the range PA = 0° – 90°, we can judge that the semi-opening angle of the ionized flow is $\approx 45°$.

The fact that the axis of the H30α pattern is roughly parallel to the axis of the cometary-shaped H II region[8] is consistent with the idea that the H II region is expanding along that axis. At the NE edge of the H30α outflow (see Fig. 9), both the apex of the comet-shaped continuum emission and the arc drawn by the water masers reveal the bow-shock of the ionized gas impacting at high speed against dense neutral material to NE. The lower intensity but larger extension of the continuum to SW, that is, the tail of the cometary H II region, is readily explained in terms of decreasing density of the ambient material towards this direction. This interpretation fits with the sparse distribution and faint emission of the methanol masers in this area and with the non-detection of water masers, whose excitation requires relatively high ambient densities, $n_{\rm H_2} \geq 10^7$ cm^{-3}.

The considerations above about the geometry of the H30α flow and its relation with the continuum emission are based on the observed $V_{\rm LSR}$ pattern only. The present ALMA data do not spatially resolve the H30α emission, so higher angular-resolution observations are needed to accurately measure the opening angle of the ionized flow and compare its structure with that of the free-free emission.

5.4. Signature of expansion of core A1

We have searched for signatures of molecular flows emerging from core A1 by imaging transitions of typical outflow tracers like SiO and ^{13}CO. The emission of these molecules towards G24.78+0.08 is extended and spatially resolved by ALMA, and the obtained images are too noisy and patchy to be used for

---

[7] The fitted size takes into account the SW tail of the H II region as well.

[8] The axes of the H30α peak distribution and the VLA 7 mm continuum emission can actually be aligned by introducing a small offset, 10 mas both to E and S, in the ALMA positions. Such an offset is consistent with the expected accuracy in the absolute positions of the ALMA data.
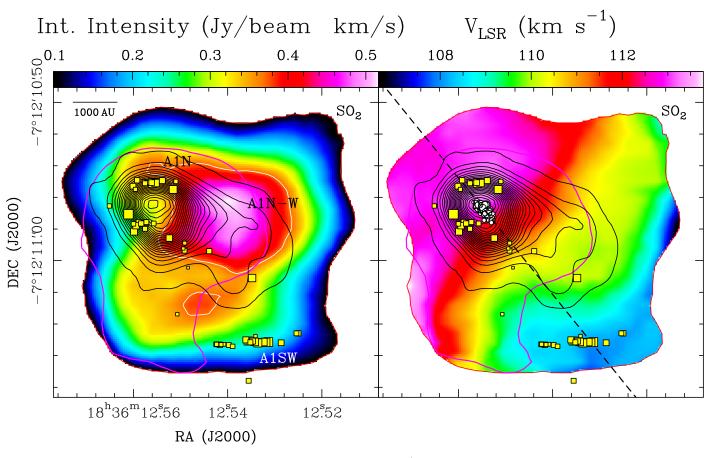
Fig. 11. Color maps showing the velocity-integrated (over the range 103–118 km s^{-1}) intensity (*left panel*) and intensity-averaged velocity (*right panel*) of the SO$_2$ v = 0 16(1,15)–15(2,14) transition in core A1. The wedges at the top of the panels give the amplitude scale of the maps. In the *left panel*, the two white contours mark the integrated intensity level of 0.37 Jy beam^{-1} km s^{-1}, and delimit two areas of prominent SO$_2$ emission. In both panels, the magenta and black contours, and the yellow squares have the same meaning as in Fig. 5. In the *right panel*, the white dots mark the channel peak positions of the H30α line emission. The dashed black line marks the axis of the spatial distribution of the H30α peaks.

outflow identification. The kinematic imprint of the fast out-flow inside the HC H II region in A1N onto the surrounding molecular gas can be effectively displayed using alternative tracers. At radii of only a few hundred AU, the expansion of the molecular envelope surrounding the ionized gas is traced by the 3D velocities of the 6.7 GHz methanol masers (see Fig. 10, upper panel). The 6.7 GHz masers in the linear pattern N of the HC H II region present relatively large proper motions (up to 12 km s^{-1}), all pointing towards NW along a direction approximately perpendicular to the axis of the ionized flow. The 6.7 GHz masers in the clusters to SE and S show smaller and less ordered proper motions, but are on average directed towards SE. Therefore, they suggest that the dense gas on the SE side of the molecular envelope is expanding away from the outflow axis, possibly at velocities on average smaller than for the NW side.

Looking at the V_{LSR} and FWHM distributions of core A1 (Figs. 5, 6 and 7, lower panels), we note two interesting features. Firstly, the area between the SW tail of the free-free emission and the region A1SW is characterized by a steep change in V_{LSR}, rapidly decreasing from N to S. Secondly, in the same area, the molecular line widths are particularly high, showing an elongated ridge (LW-ER). Moreover, the 6.7 GHz maser 3D velocities indicate that the region A1SW is moving towards S–SE with a velocity of ≈10 km s^{-1} (Fig. 5, lower-left panel). We think that these findings can be explained with fast expansion of the ionized gas to the SW. The rapid N–S change

in V_{LSR}, the increase in molecular line widths, and the linear distribution of methanol masers could originate in the shock front of the ionized gas expanding in the molecular material. Based on the intensity ratio ≳10 (see Fig.4, upper panel) of the 1.3 cm continuum emission between the core and the tail, we expect that the density of the ionized gas decreases by at least one order of magnitude in the tail, becoming about three orders of magnitude lower than that of the surrounding molecular gas. Repeating the calculation of Sect. 5.3, to account for shock velocities of ≈10 km s^{-1} (measured with the 6.7 GHz masers in A1SW), the ionized gas in the tail must flow at speeds ≳300 km s^{-1}.

We see above that the 3D motion of the molecular gas in A1N and A1SW can be interpreted in terms of expansion driven by shocks at the border of the HC H II region. In A1N-W (see Fig. 5, upper-left panel), 6.7 GHz masers are not detected and we do not know the local 3D gas velocities. However, the interaction between molecular and ionized gas can be traced using the SO$_2$ emission, a typical shock tracer. Figure 11 (left panel) shows that in A1N-W the ionized gas interacts strongly with the adjacent molecular gas. An extended layer of shocked molecular gas is produced, as mapped by the SO$_2$ emission, which reaches its maximum just inside A1N-W. The good correspondence between the spatial distributions of the SO$_2$ intensity and the gas temperature traced by CH$_3$OCHO (see Fig. 5, upper-right panel) suggests that the molecular gas in A1N-W is heated to 300–400 K in extended shocks powered by the ionized flow.
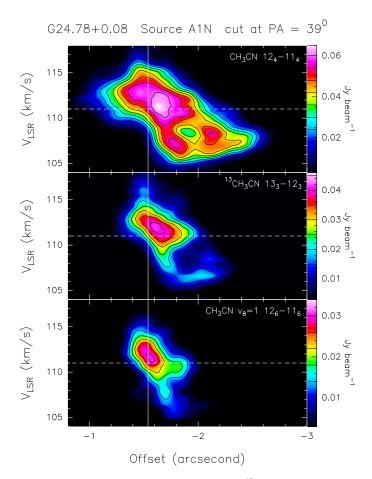
Fig. 12. P–V plots of the CH_3CN 12_4–11_4 , $^{13}CH_3CN$ 13_3–12_3 and CH_3CN v_8=1 12_6–11_6 lines are presented in the upper, middle and lower panels, respectively. The intensity scale is shown in the wedge on the right of each panel. The cut axis along which positions are evaluated is the major axis of the H30α outflow (indicated with a black dashed line in Fig. 9). To produce the P–V plots, we have averaged the emission inside a strip extending $\pm 0\farcs 3$ above and below the cut axis, including only the H II region and its surroundings.

In agreement with this interpretation, the velocity map of the SO_2 emission presents a clear SW–NE V_{LSR} gradient, approximately aligned with the direction of the H30α flow (see Fig. 11, right panel).

To further study the kinematics of the molecular gas surrounding the H II region, we have selected lines of CH_3CN (and its isotopologs) of very different optical depth and excitation, and constructed position-velocity (P–V) plots along the axis of the ionized flow (at $PA = 39°$). We have averaged the emission transversally to this axis within a strip ($0\farcs 6$ wide) small enough to reduce/exclude the contribution of the southern, more blueshifted regions A1M and A1SW (see Fig. 5). Looking at the P–V plots in Fig. 12, it is clear that a V_{LSR} gradient along the axis of the ionized flow is well detected in all the considered lines of CH_3CN (and its isotopologs), from lower energy and/or optically thicker (as the CH_3CN 12_4–11_4, with $E_u = 183$ K) to higher energy and/or optically thinner (as the CH_3CN $v_8 = 1$ 12_6–11_6, with $E_u = 771$ K) transitions. Comparing the P–V plots, it is also evident that the V_{LSR} gradient steepens with the excitation of the line, reaching the highest value (≈ 12.4 km s^{-1} arcsec^{-1}) for the most excited (CH_3CN $v_8 = 1$ 12_6–11_6) line. This might be explained by considering that the warmer (and more irradiated) molecular material is expected to be closer to the fast ionized gas, and should also move at higher velocities. This conjecture
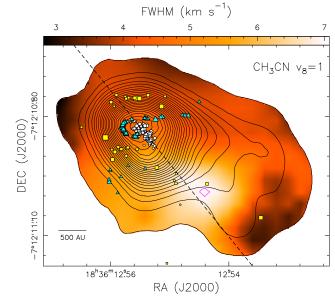
Fig. 13. Color map showing the distribution of line width determined by simultaneously fitting the emission of ten unblended, vibrationally excited transitions of CH_3CN with the XCLASS package (see Sect. 3 for details). The field of view corresponds with the area of the HC H II region in G24.78+0.08 A1N. The black contours reproduce the JVLA A-Array 1.3 cm continuum (plotting the same levels as in Fig. 4, upper panel). The magenta contour represents the level of $FWHM = 7$ km s^{-1}, and delimites the local maximum in line width LW-CS. The white dots mark the channel peak positions of the H30α line emission, and the dashed black line marks the axis of their spatial distribution. The cyan triangles and yellow squares have the same meaning as in Fig. 9.

appears to be confirmed by looking at Fig. 13, which presents the distribution of line width of vibrationally excited CH_3CN over the H II region and shows that the region LW-CS of local maximum ($\gtrsim 7$ km s^{-1}) lies just along the axis of the ionized flow, ≈ 1800 au SW of the continuum peak. The vibrationally excited lines of CH_3CN originate in warm ($\gtrsim 200$ K, see Fig. 5, upper-right panel) and turbulent molecular gas, shock-excited by the propagation of the fast ionized flow to the SW.

The new ALMA data prompt us to interpret the SW–NE V_{LSR} gradient detected in different lines of CH_3CN at variance with previous interferometric (PdBI, SMA) observations of the G24.78+0.08 A1 core (Beltrán et al. 2004, 2011). Rather than gravitationally supported rotation of a massive toroid, we interpret it as expansion of the molecular gas in core A1 associated with the fast SW–NE ionized outflow inside the HC H II region in A1N. We note here that a relevant contribution to the interpretation of the SW–NE V_{LSR} gradient in terms of a rotating toroid has been the presence of a compact molecular outflow, originally detected by Furuya et al. (2002), emerging from core A and elongated in the NW–SE direction roughly perpendicular to the V_{LSR} gradient. However, subsequent, more sensitive SMA and VLA observations (Vig et al. 2008; Beltrán et al. 2011; Codella et al. 2013) with higher angular resolution have indicated that the NW–SE molecular outflow is likely driven by a YSO inside core A2, and that there is no evidence of a molecular outflow from core A1.

As already shown in Sect. 5.2, across the whole core A1 the V_{LSR} gradient mapped in several molecular lines is directed S–N rather than SW–NE, this latter being, as discussed above, the orientation of the V_{LSR} gradient for the molecular emission emerging from the surroundings of the HC H II region only.

This different orientation of the V_{LSR} gradient is mainly due to the relevant contribution of the region of prominent molecular emission A1M (see Fig. 5, upper-left panel), located S of the HC HII region and with more blueshifted velocities. However, A1M has the same V_{LSR} as the adjacent gas closer to the HC HII region, and the S–N V_{LSR} gradient covers the same ranges in velocities and spatial separations as the SW–NE gradient. Therefore, it is straightforward to interpret the S–N V_{LSR} gradient in the same way as the SE–NW gradient, that is in terms of global expansion of the molecular core A1.

5.5. Nature of the ionized and molecular flows

The analysis performed in Sects. 5.3 and 5.4 shows that the ionized gas inside the HC HII region and the surrounding molecular gas flow along a common direction (at $PA = 39°$). In the following, we estimate the momenta of the two flows. For the ionized gas, we have derived a total mass of $\approx 5 \times 10^{-3} M_\odot$ (see Sect. 5.2) and velocities ≥ 200 km s^{-1} (see Sect. 5.1), which imply a global momentum $\geq 1 M_\odot$ km s^{-1}. Since the total mass of molecular material projected over the area of the HC HII region amounts to $2 M_\odot$ (see Sect. 5.1) and the observed V_{LSR} gradient extends over a velocity range of ± 4 km s^{-1} (see Fig. 11, left panel, and Fig. 12), we expect a global momentum in molecular gas of a few $M_\odot$ km s^{-1}. The agreement between the global momenta of the ionized and molecular flows suggests that they are associated and share a common origin.

To account for the shell-like morphology of the radio continuum and the fast expansion of the water masers at the border of the HC HII region, Moscadelli et al. (2007) proposed that the massive YSO at the center of the HC HII region emits a powerful stellar wind, with properties similar to those of the stellar winds driven by O-type ZAMS stars: mass loss rates ~ 1–$5 \times 10^{-6} M_\odot$ yr^{-1}; terminal velocities ~ 1000–3000 km s^{-1} (see, for instance, Repolust et al. 2004). The wind-driven model by Moscadelli et al. (2007) assumed a spherical geometry and derived a short timescale ≤ 80 yr for the expansion of the water maser shell. Using high, but still plausible, values for the mass loss rate, $5 \times 10^{-6} M_\odot$ yr^{-1}, and terminal velocity, 3000 km s^{-1}, the momentum delivered by the stellar wind over 80 yr amounts to $\approx 1 M_\odot$ km s^{-1}. Since this is comparable with the momenta of the ionized and molecular flows estimated above, this simple calculation shows that a powerful stellar wind could drive the motion of the ionized and molecular gas in core A1.

However, the scenario where an (isotropic) stellar wind is the engine of the ionized flow does not explain the observed bipolarity in the H30α flow, which requires some degree of collimation. An alternative interpretation – that offers the advantage of an intrinsic degree of collimation – is that the ionized and molecular gas are accelerated within a young, still compact protostellar outflow. In this respect, the "outflow-confined HII region" model (Tan & McKee 2003; Tanaka et al. 2016) could be of particular relevance in our case. This model predicts a very small jet-like HII region confined by the protostellar outflow from the massive, ionizing YSO, which could be identified with a HC HII region. The protostellar outflow is magnetically collimated; for a 20 $M_\odot$ YSO, the predicted values of mass loss rate, $\sim 10^{-5} M_\odot$ yr^{-1}, and wind terminal velocity, ~ 1000 km s^{-1}, are high enough to potentially drive the flows in the ionized and molecular gas observed in G24.78+0.08 core A1.

To distinguish among the two different scenarios, we clearly need higher-quality data. Future more sensitive JVLA continuum and higher-angular resolution ALMA line observations could allow us to map the structure and kinematics of the gas at radii of a few 100 au from the high-mass YSO, to search for an (ionized) accretion disk and unveil the collimating agent of the flows.

5.6. Excitation conditions throughout core A1

So far, we have mainly focused on the kinematics of core A1. In this section, we wish to discuss the excitation conditions of the gas using the column density and rotation temperature maps of Figs. 5, 6 and 7 (upper panels). As already noted in Sect. 4, all the derived column density maps, fitting molecular transitions of both (relatively) low (CH$_3$OCHO, ^{13}CH$_3$CN, ^{13}CH$_3$OH and CH$_3$CH$_2$CN) and high (CH$_3$CN $v_8 = 1$) energy level, are in reasonable agreement, and share the common feature of the maximum at the center of the region A1M. Over core A1, the rotation temperature maps obtained from transitions of different molecular species are also consistent, with the exception of the region A1M, where the temperature ($\gtrsim 250$ K) computed with lines of lower energy level, i.e., CH$_3$OCHO and ^{13}CH$_3$CN, is significantly higher than the value (≈ 120 K) derived with high-energy, vibrationally excited CH$_3$CN lines. In the following, we explain such a difference in terms of radiative excitation of the vibrationally excited CH$_3$CN levels.

The possibility that the vibrationally excited levels of CH$_3$CN are radiatively pumped by 27 μm radiation was originally suggested by Goldsmith et al. (1983). Using the laboratory measurement of the spontaneous decay rate of the $v_8 = 1$ band of CH$_3$CN, $A_{vib} \approx 1.6 \times 10^{-2}$ s^{-1} (Koivusaari et al. 1992), and adopting for the collision cross section the same value as for the vibrational ground state, $< \sigma v >_{vib} \approx 2 \times 10^{-10}$ cm^3 s^{-1} (Green 1986), we derive a critical density $n_{cr} \sim 10^8$ cm^{-3}. Critical densities of vibrationally excited states of other molecules typically tracing "hot cores" are comparably high, $n_{cr} > 10^9$ cm^{-3} (Wyrowski et al. 1998). The derived critical density for the vibrationally excited CH$_3$CN equals the maximum densities expected in core A1 in correspondence with the peak in column density inside the region A1M (see Fig. 5, upper-left panel), which are estimated to be a few 10^8 cm^{-3}. Therefore, in less dense regions of core A1, it is possible that the vibrationally excited lines of CH$_3$CN are not collisionally populated and efficiently excited by radiation only.

To better investigate the excitation conditions of CH$_3$CN, we have determined the vibrational temperature, T_{vib}, of the $v_8 = 1$ levels in different relevant positions of core A1. For this purpose, we have used the tool MADCUBA[9] to fit simultaneously vibrational ground ($v = 0$) and vibrationally excited ($v_8 = 1$) levels of CH$_3$CN. We selected only optically thin, unblended transitions: the CH$_3$CN $v = 0$ $J_K = 12_K$–11_K, with $K = 2, 3, 4, 5$, and the ten transitions of CH$_3$CN $v_8 = 1$ listed in Table 1. Towards the peak of the HC HII region in A1N, and the regions A1M and A1SW, we find values of T_{vib} equal to 939 ± 73 K, 643 ± 49 K, and 296 ± 19 K, respectively. From these results, it is clear that both towards the HC HII region and A1M, where $T_{vib} \gg T_{rot}$ (the latter has been derived from CH$_3$OCHO – see Fig. 5, upper-right panel), the infrared pumping is dominant over collisions. Instead, towards A1SW, where T_{vib} and the (CH$_3$OCHO) T_{rot} (200–250 K) are comparable, both collisions and radiation could be equally important in exciting the $v_8 = 1$ levels. Where radiative excitation dominates, the vibrational temperature should be close to the temperature of the

---

[9] Madrid Data Cube Analysis on Image (MADCUBA) is a software developed in the Center of Astrobiology (Madrid, INTA-CSIC) to visualize and analyze astronomical (single) spectra and data cubes (Martín et al., in prep.; Rivilla et al. 2016).

27 μm radiation pumping the vibrational levels, and our result confirms the expectation of a decrease in intensity of the MIR field with the distance from the HC H II region. We can conclude that, the differences in the fitted values of T_{rot} obtained from vibrationally excited levels of CH$_3$CN with respect to those derived from transitions of the vibrational ground state levels, have to be imputed to the radiative excitation of the vibrational levels of CH$_3$CN.

In line with this interpretation, the maximum rotational temperatures of vibrationally excited CH$_3$CN, 250–350 K, are found to be in correspondence with the HC H II region in A1N, where the local MIR field is expected to be particularly strong.

On the other hand, the maximum rotational temperatures of CH$_3$OCHO, 300–400 K, are observed not towards the center of the HC H II region but towards A1N-W, at the same position as the intensity peak of the SO$_2$ emission (compare Fig. 5, upper-right panel, with Fig. 11, left panel). It is plausible that the temperature distribution over core A1 reflects the heating in shocks induced by the fast SW–NE ionized flow onto the surrounding environment.

The region A1M has several characteristics in common with the region A1N-W. Firstly, in both locations the gas temperature and density, as traced by CH$_3$OCHO (see Fig. 5, upper panels), increase to comparable values. The peak density in A1M is about twice that of A1N-W, and the CH$_3$OCHO temperature in A1M is ≈30% lower than in A1N-W. Secondly, over core A1, beside the main peak in A1N-W, the SO$_2$ emission presents also a secondary maximum, which is located close to A1M (see Fig. 11, left panel). Based on these facts, we propose that the region A1M is also heated by shocks, induced by the expansion of the ionized gas of the H II region to S–SE. In partial support of this interpretation, Fig. 5 (upper-left panel) shows that the region A1M is adjacent to a small southern spur of the continuum emission that protrudes towards the column density peak at the center of A1M.

Even if we propose that the region A1M is mainly heated by external shocks, we cannot exclude the contribution of internal star-formation activity. In this region, the non-detection of free-free emission above the threshold of 0.1 mJy beam^{-1} sets an upper limit of 13 $M_\odot$ for the mass of any (ZAMS) star. If stars are forming inside A1M, it is more likely that they are of low and/or intermediate mass, which agrees with the non-detection of water masers and the detection of only a weak 6.7 GHz maser in this region. The distributions in density, temperature, V_{LSR} and velocity line width across A1M (see Fig. 5) do not provide hints of substructures, but the angular resolution of the ALMA observations could be insufficient for their identification. With the present data, there is no indication for molecular outflows originating from A1M, either. This region is the densest reservoir of molecular gas in core A1 (≈2 $M_\odot$ over ≈1000 au) and the most likely site for finding new YSOs (other than the massive star exciting the HC H II region in A1N). Future ALMA observations, with higher sensitivity and angular resolution, will allow us to investigate the physical conditions and kinematics of this region in more detail, and to verify the presence of on-going star formation.

Finally, we wish to consider the properties of the region A1SW, where a linear distribution of relatively bright 6.7 GHz masers is observed (see Fig. 5). The total molecular mass in this area is estimated to be only ≈0.2 $M_\odot$ (see Sect. 5.1). We have proposed that the motion towards S–SE of the 6.7 GHz masers is driven by the rapid expansion of the ionized gas in the SW tail of the continuum emission (see Sect. 5.4). Methanol masers are predicted to be radiatively pumped by 20–30 μm photons (see, for instance, Moscadelli et al. 2017) and are typical

signatures of massive YSOs. However, the non-detection of free-free emission and the small molecular content would lead us to conclude that no massive YSO is inside A1SW. We think that the 6.7 GHz masers of this region can be excited by the radiation of the massive star in A1N, either flowing directly from the star to the SW along the cavity excavated by the ionized flow, or reprocessed by the dust at the cavity wall. From the values derived in A1SW for the vibrational temperature of CH$_3$CN, 296±19 K, and the gas temperature, 200–250 K (as traced by CH$_3$OCHO – see Fig. 5, upper-right panel), we can infer that, in this region, the temperature of the 27 μm radiation should vary in the range 300–400 K. According to the models of Cragg et al. (2005; see their Fig. 2), this is the range of values for the dust (and radiation) temperature, over which the 6.7 GHz masers reach the maximum intensities (or, equivalently, the highest pumping efficiencies). In addition, Fig. 5 (upper-left panel) shows that the A1SW maser cluster is located where the farthest SW portion of the ionized flow hits molecular material of relatively high column density ($N_{tot} \gtrsim 10^{17}$ cm^{-2} for CH$_3$OCHO), resulting in stronger amplification of the 6.7 GHz masers.

6. Conclusions

This article combines high-angular resolution ALMA Cycle-2 1.4 mm observations of continuum and line emissions with multi-epoch VLBI water 22 GHz and methanol 6.7 GHz maser data to study the physical conditions and kinematics of the most prominent molecular core, A1 (size ≈ 6600 au), in the star-forming region G24.78+0.08. The ALMA data have been analyzed with the tools STATCONT to determine the continuum level of the observed spectra, and XCLASS to fit the emission of multiple lines of a given molecular species and produce density, temperature, velocity and line-width maps. The maps are obtained by fitting (relatively) low-energy (30 K $\leq E_u/k \leq$ 320 K) transitions of CH$_3$OCHO, ^{13}CH$_3$CN, ^{13}CH$_3$OH, and CH$_3$CH$_2$CN, and high-energy (590 K $\leq E_u/k \leq$ 780 K) transitions of vibrationally excited CH$_3$CN.

The 1.4 mm continuum is dominated by the intense free-free emission from the HC H II region (size ≈ 1000 au) observed N of core A1 (region A1N). Employing the H30α line, we reveal a fast ($\Delta V_{LSR} \approx 60$ km s^{-1}), bipolar (blue(red)-shifted to SW(NE), PA = 39°) flow in the ionized gas. We infer that the ionized gas moves at velocities $\geq$200 km s^{-1}, much higher than its sound speed (~10 km s^{-1}), and is likely accelerated by a powerful wind/outflow ejected from the O-type star at the center of the HC H II region. The fast-moving ionized gas shocks against the dense molecular material surrounding the H II region, and this interaction appears to be responsible for the excitation of most of the gas throughout the whole core A1.

The molecular gas surrounding the HC H II region moves in concordance with the ionized gas, sharing the same direction of motion and presenting a similar global momentum. The V_{LSR} maps and P–V plots of several shock and high-density tracers (like SO$_2$ and CH$_3$CN, respectively) show a well-defined V_{LSR} gradient directed SW–NE, parallel to the axis of the ionized flow. Over the whole core A1, the V_{LSR} maps of the 1.4 mm molecular lines show a gradient (amplitude ≈9 km s^{-1} arcsec^{-1} or ≈0.3 km s^{-1} mpc^{-1}) directed approximately S–N. Rather than gravitationally supported rotation of a massive toroid, we interpret the S–N V_{LSR} gradient observed throughout the core extent as a relatively slow expansion of core A1.

References

Beltrán, M. T. & de Wit W. J. 2016, A&ARv, 24, 6
Beltrán, M. T., Cesaroni, R., Neri, R., et al. 2004, ApJ, 601, L187
Beltrán, M. T., Cesaroni, R., Neri, R., et al. 2005, A&A, 435, 901
Beltrán, M. T., Cesaroni, R., Codella, C., et al. 2006, Nature, 443, 427
Beltrán, M. T., Cesaroni, R., Moscadelli, L., & Codella, C. 2007, A&A, 471, L13
Beltrán, M. T., Cesaroni, R., Zhang, Q., et al. 2011, A&A, 532, A91
Beltrán, M. T., Sánchez-Monge, Á., Cesaroni, R., et al. 2014, A&A, 571, A52
Beuther, H. & Shepherd, D. 2005, in Cores to Clusters: Star Formation with Next Generation Telescopes, eds. M. S. N. Kumar, M. Tafalla, & P. Caselli, 105
Briggs, D. S. 1995, Bull. Am. Astron. Soc, AAS Meetings Abstracts, 27, 1444
Cesaroni, R., Sánchez-Monge, Á., Beltrán, M. T., et al. 2017, A&A, 602, A59
Codella, C., Beltrán, M. T., Cesaroni, R., et al. 2013, A&A, 550, A81
Cragg, D. M., Sobolev, A. M., & Godfrey, P. D. 2005, MNRAS, 360, 533
Furuya, R. S., Cesaroni, R., Codella, C., et al. 2002, A&A, 390, L1
Goddi, C. & Moscadelli, L. 2006, A&A, 447, 577
Goddi, C., Moscadelli, L., Alef, W., et al. 2005, A&A, 432, 161
Goldsmith, P. F., Krotkov, R., Snell, R. L., Brown, R. D., & Godfrey, P. 1983, ApJ, 274, 184
Green, S. 1986, ApJ, 309, 331
Ilee, J. D., Cyganowski, C. J., Nazari, P., et al. 2016, MNRAS, 462, 4386
Johnston, K. G., Robitaille, T. P., Beuther, H., et al. 2015, ApJ, 813, L19
Keto, E. & Klaassen, P. 2008, ApJ, 678, L109
Koivusaari, M., Horneman, V. M., & Anttila, R. 1992, J. Mol. Sp., 152, 377
Kuiper, R., Turner, N. J., & Yorke, H. W. 2016, ApJ, 832, 40
Masson, C. R. & Chernin, L. M. 1993, ApJ, 414, 230
McMullin, J. P., Waters, B., Schiebel, D., Young, W., & Golap, K. 2007, Astronomical Data Analysis Software and Systems XVI, eds. R. A. Shaw, F. Hill, & D. J. Bell, ASP Conf. Ser. 376, 127
Möller, T., Endres, C., & Schilke, P. 2017, A&A, 598, A7
Moscadelli, L. & Goddi, C. 2014, A&A, 566, A150
Moscadelli, L., Goddi, C., Cesaroni, R., Beltrán, M. T., & Furuya, R. S. 2007, A&A, 472, 867
Moscadelli, L., Cesaroni, R., Rioja, M. J., Dodson, R., & Reid, M. J. 2011, A&A, 526, A66
Moscadelli, L., Li, J. J., Cesaroni, R., et al. 2013, A&A, 549, A122
Moscadelli, L., Sánchez-Monge, Á., Goddi, C., et al. 2016, A&A, 585, A71
Moscadelli, L., Sanna, A., Goddi, C., et al. 2017, A&A, 600, L8
Ossenkopf, V. & Henning, T. 1994, A&A, 291, 943
Panagia, N. 1973, AJ, 78, 929
Peters, T., Banerjee, R., Klessen, R. S., & Mac Low M.-M. 2011, ApJ, 729, 72
Peters, T., Klaassen, P. D., Mac Low, M.-M., et al. 2014, ApJ, 788, 14
Purser, S. J. D., Lumsden, S. L., Hoare, M. G., et al. 2016, MNRAS, 460, 1039
Reid, M. J., Schneps, M. H., Moran, J. M., et al. 1988, ApJ, 330, 809
Repolust, T., Puls, J., & Herrero, A. 2004, A&A, 415, 349
Rivilla, V. M., Beltrán, M. T., Cesaroni, R., et al. 2017a, A&A, 598, A59
Rivilla, V. M., Beltrán, M. T., Martín-Pintado, J., et al. 2017b, A&A, 599, A26
Rivilla, V. M., Fontani, F., Beltrán, M. T., et al. 2016, ApJ, 826, 161
Rosero, V., Hofner, P., Claussen, M., et al. 2016, ApJS, 227, 25
Sánchez-Monge, Á., Cesaroni, R., Beltrán, M. T., et al. 2013, A&A, 552, L10
Sanchez-Monge, A., Schilke, P., Ginsburg, A., Cesaroni, R., & Schmiedeke, A. 2018, A&A, 609, A101
Sanna, A., Moscadelli, L., Cesaroni, R., et al. 2010a, A&A, 517, A71
Sanna, A., Moscadelli, L., Cesaroni, R., et al. 2010b, A&A, 517, A78
Sanna, A., Reid, M. J., Carrasco-González, C., et al. 2012, ApJ, 745, 191
Tan, J. C., & McKee, C. F. 2003, ArXiv e-prints [arXiv:astro-ph/0309139]
Tan, J. C., Beltrán, M. T., Caselli, P., et al. 2014, Protostars and Planets VI, 149
Tanaka, K. E. I., Tan, J. C., & Zhang, Y. 2016, ApJ, 818, 52
Tenorio-Tagle, G. 1979, A&A, 71, 59
Vaidya, B., Fendt, C., Beuther, H., & Porth, O. 2011, ApJ, 742, 56
Vig, S., Cesaroni, R., Testi, L., Beltrán, M. T., & Codella, C. 2008, A&A, 488, 605
Wyrowski, F., Schilke, P., & Walmsley, M. 1998, in Star Formation with the Infrared Space Observatory, eds. J. Yun, & L. Liseau, ASP Conf. Ser., 132, 438

Appendix A: Model of rigid rotation for core A1

Adopting a simple model of rigid rotation, we wish to determine the amplitude and orientation of the angular velocity vector which best reproduces the distribution of V_{LSR} and proper motions observed in core A1 with thermal and maser tracers. We indicate with W the angular velocity vector, and with W_x, W_y, and W_z its components along the E, N and line of sight directions, respectively. If R is the position vector from the barycenter of the 6.7 GHz maser cluster A1N to the barycenter of the cluster A1SW, the rotation velocity V_{rot} of A1SW around A1N can be expressed with $V_{rot} = W \wedge R$. By means of our multi-epoch EVN observations of the 6.7 GHz masers in A1, we accurately measure both the projection of R on the sky, and the relative velocity V of the maser cluster A1SW with respect to the cluster A1N (see Table B.1). Naming the E, N, and line of sight components of R and V with R_x, R_y, and R_z, and V_x, V_y, and V_z, respectively, we have: $R_x = -327 \pm 2$ mas ; $R_y = -405 \pm 3$ mas; $V_x = 4.4 \pm 1.0$ km s^{-1}; $V_y = -9.8 \pm 0.9$ km s^{-1}; $V_z = -5.7 \pm 0.2$ km s^{-1}.

To model the kinematics of core A1 in terms of rigid rotation, we impose $V_{rot} = W \wedge R = V$. Since V_{LSR} in core A1 increase regularly from S to N and are almost constant along E–W, for simplicity we take $W_y = 0$. With this premise, the vector relation above can be easily solved for the W components W_x and W_z, and for the R component R_z. We derive $W_x = 14.2 \pm 0.5$ km s^{-1} and $W_z = 11 \pm 3$ km s^{-1}, and $R_z = 440 \pm 140$ mas. The amplitude and the line of sight inclination of W are $|W| = 18 \pm 3$ km s^{-1} arcsec^{-1} and $i = 53° \pm 8°$, respectively.

Appendix B: Additional table

Table B.1. 6.7 GHz CH_3OH maser parameters for G24.78+0.08 A1.

Feature number	Epochs[a] of detection	I_{peak} (Jy beam^{-1})	V_{LSR} (km s^{-1})	Δx (mas)	Δy (mas)	V_x (km s^{-1})	V_y (km s^{-1})
				Cluster A1N			
1	1,2,3	81.19	113.4	0.00±0.00	0.00±0.00	1.1± 0.7	−2.1± 0.8
2	1,2,3	20.18	114.1	−76.43±0.08	98.71±0.08	−2.4± 0.7	3.0± 0.8
3	1,2,3	5.39	114.8	−141.18±0.08	78.18±0.08	−4.9± 0.7	−0.4± 0.8
4[b]	1,2,3	3.87	114.1	−85.63±0.10	98.19±0.12	...	...
5	1,2,3	1.48	114.4	−17.70±0.11	−55.32±0.13	3.8± 0.9	−7.1± 1.0
6	2	1.34	108.1	−391.01±0.25	−202.82±0.23	...	...
7	1,2,3	1.00	113.0	−23.95±0.12	−36.47±0.13	−2.9± 0.9	−0.6± 1.0
8	1,2,3	0.85	114.2	−38.72±0.17	−29.44±0.20	9.3± 1.0	5.3± 1.3
9	1,2,3	0.73	110.2	−129.04±0.19	−75.49±0.23	1.3± 1.4	−4.3± 1.7
10	3	0.72	113.5	−74.69±0.21	97.88±0.29	...	...
11	1,2,3	0.61	113.1	−106.98±0.25	106.19±0.34	−8.0± 1.8	7.9± 2.4
12	1,2	0.44	113.7	−14.33±0.22	88.61±0.28	...	...
13	1,2,3	0.43	113.2	−55.02±0.31	−26.37±0.36	11.1± 1.9	0.5± 2.3
14	2,3	0.32	113.6	−52.07±0.27	97.14±0.47	...	...
15	1,2,3	0.28	114.8	−27.68±0.27	106.88±0.36	−5.2± 1.7	5.3± 2.5
16	3	0.28	114.6	−41.37±0.15	−31.36±0.18	...	...
17	1,2,3	0.27	116.6	−255.38±0.13	−116.67±0.16	−2.3± 1.3	2.8± 1.6
18	1,2,3	0.23	115.1	−32.27±0.26	−24.14±0.32	−0.4± 1.5	−5.8± 2.0
19	2	0.18	112.9	−16.29±0.18	−31.66±0.37	...	...
20	1,2,3	0.18	114.7	−52.42±0.51	−46.18±0.70	8.7± 2.7	1.9± 3.9
21	2	0.18	113.6	−58.58±0.60	98.75±1.00	...	...
22	3	0.18	113.6	−57.83±0.27	−27.14±0.33	...	...
23	2	0.17	114.1	−79.88±0.39	−30.63±0.53	...	...
24	1,2,3	0.15	108.9	−177.28±0.24	−115.33±0.32	3.7± 2.0	−3.4± 2.7
25	2,3	0.11	115.0	−149.75±0.28	102.65±0.44	...	...
26[b]	1,2,3	0.11	112.8	60.09±0.42	25.85±0.59	...	...
27	3	0.10	114.7	−23.32±0.35	76.34±0.54	...	...
28	1,2,3	0.09	115.1	−49.71±0.38	102.99±0.44	−7.2± 4.4	9.8± 3.9
29	3	0.07	114.8	−155.87±0.55	−318.19±0.57	...	...
30	1,2,3	0.07	109.4	−177.82±0.51	−91.35±0.68	−2.3± 4.0	−11.4± 5.7
31	3	0.06	109.2	−174.72±0.38	−110.64±0.61	...	...
32	3	0.04	109.2	−189.65±0.61	−170.96±0.49	...	...
				Cluster A1SW			
1	1,2,3	18.97	107.7	−441.61±0.09	−404.01±0.10	2.5± 0.8	−8.4± 0.9
2	1,2,3	11.43	107.8	−433.43±0.09	−404.94±0.10	5.8± 0.7	−11.2± 0.8
3	1,2,3	7.73	108.0	−408.71±0.09	−406.65±0.09	−0.9± 0.7	−10.8± 0.8
4	1,2,3	6.04	108.0	−377.97±0.11	−400.50±0.10	9.7± 0.8	−8.3± 0.9
5	2,3	4.67	108.0	−382.91±0.09	−402.05±0.10	...	...
6	1,2,3	3.70	108.3	−426.44±0.08	−403.91±0.09	1.6± 0.7	−10.2± 0.8
7	1,2,3	2.79	108.2	−398.99±0.11	−403.38±0.12	−2.8± 0.9	−9.4± 1.0
8	3	1.36	107.7	−436.89±0.23	−656.05±0.17	...	...
9	2	0.96	108.1	−393.44±0.29	−603.90±0.26	...	...
10	2	0.74	108.1	−418.27±0.39	−608.02±0.31	...	...
11	3	0.65	108.2	−392.87±0.12	−403.05±0.14	...	...
12	2	0.46	108.2	−406.98±0.36	−605.24±0.51	...	...
13	1,2,3	0.44	107.2	−482.45±0.16	−406.38±0.18	−1.2± 1.2	−11.0± 1.3
14	3	0.39	108.4	−372.17±0.17	−399.04±0.15	...	...
15	1,2,3	0.21	108.7	−536.40±0.25	−376.26±0.21	7.5± 2.3	−10.3± 1.9

Notes. [a]The three observing epochs are: 1) 2007 March 20; 2) 2009 March 12; 3) 2012 November 3. [b]Feature with not reliable proper motion, even if observed at three epochs. Column 1 gives the feature label number; Col. 2 lists the observing epochs at which the feature was detected; Cols. 3 and 4 provide the intensity of the strongest spot and the intensity-weighted LSR velocity, respectively, averaged over the observing epochs; Cols. 5 and 6 give the position offsets (with the associated errors) along the RA and Dec axes, relative to the persistent feature #1 of cluster A1N, measured at the first epoch of detection; Cols. 7 and 8 give the components of the relative proper motion (with the associated errors) along the RA and Dec axes, measured with respect to the reference feature #0-A1N (the "center of motion" of cluster A1N). The absolute position of the reference feature #1 in cluster A1N at the observing epoch on March 20, 2007, is: RA (J2000) = $18^h36^m12^s.5625$, Dec (J2000) = $-7°12'10''.811$, with an accuracy of ±1 mas.

Table B.1. continued.

Feature number	Epochs[a] of detection	I_{peak} (Jy beam^{-1})	V_{LSR} (km s^{-1})	Δx (mas)	Δy (mas)	V_x (km s^{-1})	V_y (km s^{-1})
16	3	0.20	107.4	−386.48±0.36	−406.75±0.29	...	...
17	2	0.19	108.6	−530.89±0.24	−377.59±0.31	...	...
18	1,2,3	0.17	106.9	−288.59±0.39	−412.53±0.27	8.2± 3.8	−9.5± 2.5
19	2	0.15	108.4	−380.00±0.47	−527.35±0.66	...	...
20	1,2,3	0.11	107.1	−316.94±0.66	−413.64±0.62	−0.6± 5.0	−9.2± 3.9
21	2	0.09	107.1	−301.78±0.49	−412.40±0.58	...	...
22	1,2,3	0.08	106.9	−329.04±0.95	−417.53±0.96	13.5± 6.8	−9.5± 5.6
23	2	0.08	106.8	−277.69±0.61	−412.23±0.69	...	...
24	3	0.07	106.8	−279.93±0.67	−412.96±0.33	...	...
25	3	0.06	107.1	−293.87±0.83	−414.17±0.46	...	...
26	1	0.05	106.4	−401.51±0.62	−384.93±0.78	...	...
Centers of Motion							
0-A1N	1,2,3	...	113.4	−77.06±0.08	0.01±0.10	0.0± 0.0	0.0± 0.0
0-A1SW	1,2,3	...	107.7	−403.69±0.13	−404.52±0.12	4.4± 1.0	−9.8± 0.9